Testing the modern merger hypothesis via the assembly of massive blue elliptical galaxies in the local Universe

Tim Haines,[1,2]⋆† D. H. McIntosh,[2] S. F. Sánchez,[3] C. Tremonti[1] and G. Rudnick[4]

[1]*Department of Astronomy, University of Wisconsin–Madison, 475 N. Charter Street, Madison, WI 53706-1582, USA*
[2]*Department of Physics and Astronomy, University of Missouri–Kansas City, 5110 Rockhill Road, Kansas City, MO 64110, USA*
[3]*Instituto de Astronomía, Universidad Nacional Autonóma de Mexico, A.P. 70-264, 04510 México, D.F., Mexico*
[4]*Department of Physics and Astronomy, The University of Kansas, Malott room 1082, 1251 Wescoe Hall Drive, Lawrence, KS 66045, USA*

ABSTRACT

The modern merger hypothesis offers a method of forming a new elliptical galaxy through merging two equal-mass, gas-rich disc galaxies fuelling a nuclear starburst followed by efficient quenching and dynamical stabilization. A key prediction of this scenario is a central concentration of young stars during the brief phase of morphological transformation from highly disturbed remnant to new elliptical galaxy. To test this aspect of the merger hypothesis, we use integral field spectroscopy to track the stellar Balmer absorption and 4000-Å break strength indices as a function of galactic radius for 12 massive ($M_* \geq 10^{10}\,\mathrm{M_\odot}$), nearby ($z \leq 0.03$), visually-selected plausible new ellipticals with blue-cloud optical colours and varying degrees of morphological peculiarities. We find that these index values and their radial dependence correlate with specific morphological features such that the most disturbed galaxies have the smallest 4000-Å break strengths and the largest Balmer absorption values. Overall, two-thirds of our sample are inconsistent with the predictions of the modern merger hypothesis. Of these eight, half exhibit signatures consistent with recent minor merger interactions. The other half have star formation histories similar to local, quiescent early-type galaxies. Of the remaining four galaxies, three have the strong morphological disturbances and star-forming optical colours consistent with being remnants of recent, gas-rich major mergers, but exhibit a weak, central burst consistent with forming ∼5 per cent of their stars. The final galaxy possesses spectroscopic signatures of a strong, centrally concentrated starburst and quiescent core optical colours indicative of recent quenching (i.e. a post-starburst signature) as prescribed by the modern merger hypothesis.

Key words: galaxies: evolution – galaxies: peculiar – galaxies: star formation.

1 INTRODUCTION

The stellar growth of high-mass ($>10^{10}\,\mathrm{M_\odot}\,h^{-2}$), quiescent (non-star-forming) galaxies remains an important topic in galaxy evolution studies. Large and deep redshift surveys have conclusively shown that these red galaxies have grown significantly since at least redshift $z \sim 2$–3 in terms of both their number density (e.g. Bell et al. 2004a; Brown et al. 2007; Martin et al. 2007; Brammer et al. 2009) and average sizes at a fixed stellar mass (Khochfar &

Silk 2006; Trujillo et al. 2006, 2007; Lee et al. 2013). The observed build-up of this population and its conserved preponderance of early-type galaxy (ETG) morphologies at different epochs (Bell et al. 2004b, 2012; Blanton 2006) requires a process (or sequence of processes) which both increases the number of galaxies with early-type morphologies *and* quenches star formation. The currently accepted explanation for this phenomenon is the so-called blue-to-red migration (Faber et al. 2007; Eliche-Moral et al. 2010; Gonçalves et al. 2012) which posits that the transformation of star-forming (blue) disc galaxies into quiescent, red ETGs is responsible for the increasing population of red sequence galaxies over cosmic time. One possible, but well-accepted, mechanism driving the blue-to-red migration is the modern merger hypothesis (Hopkins et al. 2008b). Under this model, a new massive quiescent elliptical galaxy is built by transforming two star-forming disc galaxies into one concentrated quiescent red ETG via a gas-rich major (i.e. nearly equal mass) merger.

Yet, in detail, the red ETG population contains myriad morphological types in detail from early-type spiral discs, to lenticular (S0) galaxies, to the well-known dichotomy of ellipticals (e.g. Kormendy 2009), making disentangling which migration processes are dominant a daunting task that likely depends on galaxy morphology, mass, environment, and redshift. We have made progress in the local Universe by focusing on the redwards migration of pure-spheroid elliptical galaxies (McIntosh et al. 2014, hereafter, M14). This choice is motivated by the fact that the formation of new ellipticals is theoretically tied to a *single* mechanism that both transforms discs (e.g. major merging, Toomre & Toomre 1972; Barnes 1992, and references therein) and is hierarchically motivated (White & Rees 1978; Kauffmann, White & Guiderdoni 1993).

Simulations of gas-rich major mergers provide a key prediction which allows us to qualitatively identify major merger remnants. During the merging process, gravitational torques deposit cold gas in the centre of the remnant and produce a centrally concentrated burst of star formation (Barnes & Hernquist 1991, 1996; Mihos & Hernquist 1996). According to the modern merger hypothesis, this is quickly followed by the ignition of an active galactic nucleus (AGN) which ultimately quenches star formation (Springel, Di Matteo & Hernquist 2005; Schawinski et al. 2007, 2010) and forms a quiescent elliptical galaxy (Hopkins et al. 2006, 2008a). This is supported by the bluer colours of ETGs hosting an AGN, compared with their non-active counterparts (Sánchez et al. 2004). The merging process finally produces a relaxed remnant with the structure and kinematics of observed moderate-mass spheroidal galaxies (Cox et al. 2006; Naab, Khochfar & Burkert 2006).

We, therefore, anticipate ellipticals which are plausible remnants of recent gas-rich mergers to have bluer colours as compared to their 'normal' counterparts on the colour–mass relation due to recent, enhanced star formation. Such blue ellipticals are rare. For example, Fukugita et al. (2004) found 2 of the 210 ellipticals in their sample of 1600 bright galaxies from the Sloan Digital Sky Survey (SDSS) at $z < 0.12$ to be blue ellipticals, M14 found 1602 blue ellipticals in their complete sample of 63 454 massive ($M_* > 10^{10} \, \mathrm{M}_\odot \, h^{-2}$) galaxies at $z < 0.08$, and Lee, Lee & Hwang (2006) found 29 in their sample of 1949 galaxies with spectroscopic redshifts $\lesssim 0.4$ in the Hubble GOODS fields. Despite their rarity, these galaxies are important as they build the transition from star-forming discs in the blue cloud to massive, quiescent ellipticals on the red sequence (Bell et al. 2007). The robust sample of blue elliptical galaxies seen in M14 provides a good starting point for testing methods to distinguish recent elliptical mass assembly.

Over the last decade, spatially-resolved spectroscopic surveys such as SAURON (Bacon et al. 2001) and ATLAS3D (Cappellari et al. 2011) have drastically enhanced our understanding of the content and structure of cluster and field ellipticals. Likewise, projects such as PINGS (Rosales-Ortega et al. 2010), TYPHOON (Sturch & Madore 2012), and the CALIFA survey (Sánchez et al. 2012) have provided an unprecedented level of detail in spiral galaxies. Aside from serendipitous discoveries (e.g. Fukugita et al. 2004), little work has been brought forth from the population of blue elliptical galaxies. Further, previous studies of these galaxies have been limited to evaluating only the central regions (e.g. Schawinski et al. 2009; Tojeiro et al. 2013) which provides a narrow perspective of the mass assembly history. In this work, we propose to analyse the 4000-Å break strength and Balmer absorption line indices out to ∼3 half-light radii (coverage previously only achieved for red elliptical galaxies, e.g. Weijmans et al. 2009) to examine the spatial star formation histories (SFHs) of this rare, but important population of elliptical galaxies in the local Universe.
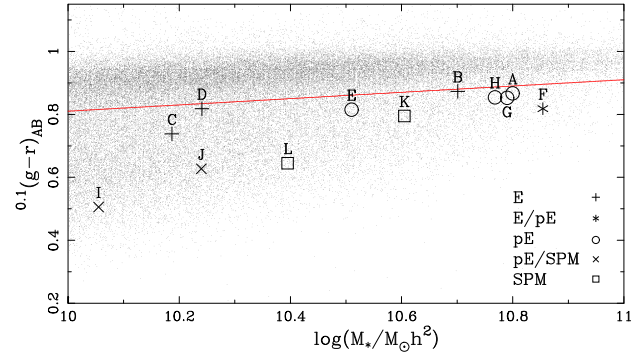

Figure 1. Colour–mass diagram for the 63 454 nearby ($0.01 \le z \le 0.08$), high-mass ($M_* \ge 10^{10} \, \mathrm{M}_\odot \, h^{-2}$) SDSS DR4 galaxies from M14 with our sample of 12 blue ellipticals overlaid. The red line shows the M14 colour cut, symbols represent visual classifications from M14. Refer to Table 1 for letter labels. A color version is available in the online journal.

Our paper is organized as follows. Section 2 details our sample selection, observation set-ups, and data reduction pipeline. Section 3 outlines our model construction. In Section 4, we provide results from our comparison of the spatially resolved spectra to a suite of SFH models. Section 5 contains the discussion of our results. Finally, in Section 6 we provide a summary and conclusions. Throughout this paper we calculate comoving distances in the Λ-cold-dark-matter concordance cosmology with $\Omega_m = 0.3$, $\Omega_\Lambda = 0.7$, and assume a Hubble constant[1] of $H_0 = 70 \, \mathrm{km \, s^{-1} \, Mpc^{-1}}$. Magnitudes from the SDSS (York et al. 2000) are on the AB system such that $m_{AB} = m + \Delta m$, where $\Delta m = (-0.036, +0.012, +0.010, +0.028, +0.040)$ for (u, g, r, i, z) (Yang et al. 2007).

2 DATA SAMPLE AND OBSERVATIONS

2.1 Sample selection

To test the prediction of the modern merger hypothesis that gas-rich major mergers lead to the construction of massive ellipticals with temporarily blue colours, we acquire observationally intensive integral field unit (IFU) spectroscopy using long exposure times to obtain spatially resolved spectra beyond the bright central bulge. We then use the $H\delta_A$ and $H\gamma_A$ Lick indices and the narrow-band 4000 Å break to map the recent SFHs as a function of galactic radius for a collection of visually-classified[2] plausible new ellipticals provided in M14. Using the New York University Value-Added Galaxy Catalogue (NYU-VAGC; Blanton et al. 2005) based on the SDSS Data Release 4 (DR4; Adelman-McCarthy et al. 2006), M14 construct a complete sample of nearby ($0.01 \le z \le 0.08$), high-mass ($M_* \ge 10^{10} \, \mathrm{M}_\odot \, h^{-2}$) galaxies. Using the rest-frame ($g - r$) Petrosian colours, the absolute r-band magnitudes, and the Bell et al. (2003) M/L prescription to measure stellar mass, they apply the empirical colour cut $^{0.1}(g - r) \le 0.81 + 0.1[\log_{10}(M_{gal,*}/\mathrm{M}_\odot \, h^{-2}) - 10.0]$ to select blue-cloud galaxies (see Fig. 1) where the colours have been k-corrected to $z = 0.1$. They isolate early-type (spheroid-dominated) galaxies using the common r-band concentration cut of $R_{90}/R_{50} \ge 2.6$

---

[1] The stellar masses from M14 are calculated assuming $H_0 = 100h$.

[2] The morphological classifications of M14 were determined by manual inspection of the images by people. Here and throughout the paper, we use the phrase 'visually-classified' to mean classified 'by eye'.

(Strateva et al. 2001), where R_{90} (R_{50}) is the radius inside which 90 per cent (50 per cent) of the light is contained to produce a set of 8403 unusually blue ETGs.

M14 then use visual classification with careful morphological inspection to identify plausible new merger remnants from this set of blue ETGs. Visual inspection further allows them to remove contamination by bulge-dominated spirals (S) and inclined discs (iD), plus galaxies with uncertain morphology (U), and galaxies affected by artefacts. Their final catalogue consists of 1602 massive, blue elliptical (E, 85 per cent), peculiar elliptical (pE, 8 per cent), and spheroidal post-merger (SPM, 7 per cent) galaxies with high classifier-to-classifier agreement, defined as a minimum of three out of four classifiers in accord. The details of these identifications and their robustness are described in detail in M14. Briefly, the E, pE, and SPM types represent three morphological bins that plausibly span a *qualitative* time sequence since merging (assuming that all blue elliptical galaxies are derived from gas-rich major merging). At one extreme (E), galaxies appear to be dynamically relaxed ellipticals with little or no evidence of recent tidal activity, contrasted by those at the other extreme which appear to be freshly coalesced with very disturbed morphologies (SPM). In between the two extremes (pE), we find galaxies which appear to be relaxed ellipticals with either a modest external morphological peculiarity (e.g. a loop or fan feature) or an internal structure like a dust lane. We parametrize the level of visual tidal features by defining a plausible post-merger type, T_{ppm}, for each blue ETG based on the sum of its four classifications weighted as follows:

$$T_{ppm} = \sum_{i=1}^{4} w_{c,i}, \tag{1}$$

where $w_{c,i}$ is the ith classification such that $w_c = -1$ (S/iD), -0.5 (U), 1 (E), 2 (pE), and 3 (SPM); e.g. $T_{ppm} = 8$ for four-way pE agreement. We use negative weights to distinguish definite discs and uncertain classifications from (positive w_c) plausible post-merger systems. We investigate a subset of the 8403 blue ETGs from M14 using a relaxed classifier agreement such that $T_{ppm} \geq 2.0$ to produce a sample of 1915 E (71 per cent), pE (6 per cent), SPM (6 per cent), plus 17 per cent with combinations of E+pE+SPM classifications (i.e. classifiers agree that these objects are not S or iD despite disagreement over specific plausible post-merger type). For example, nyu100917 appears to be a relatively smooth elliptical with a large loop structure (see Fig. 2). The classifiers in M14 were evenly split between the pE and SPM classification: falling below the 75 per cent classifier agreement requirement. Using our relaxed classifier allows this galaxy to be included in our sample.

To maximize spatial coverage of the spectra, we require each galaxy to fill the field of view (FOV) of its respective spectrograph (each spectrograph used in this work is ~70 arcsec on a side) in one of two ways: (i) twice the galaxy's $R_{90} \simeq 70$ arcsec or (ii) the galaxy has loops, arms, or other structures which extend beyond its main body to fill the FOV. These requirements reduce the range of redshifts for our targets to $z \lesssim 0.03$ and provide a sample of 111 E (57 per cent), pE (11 per cent), SPM (10 per cent), and other ($T_{ppm} \geq 2$, 23 per cent) galaxies. Based on observational availability, we select a set of 12 (3 E, 3 pE, 2 SPM, and 4 other) which nearly equally sample the morphology space while also selecting interesting candidates for unique SFHs based on a range of morphological details such as circumnuclear blue rings or large dust features. In Table 1, we list physical characteristics and morphological classifications for our sample.

In Fig. 1, we show our sample in the colour–mass plane using the SDSS ($g-r$) colours k-corrected to $z = 0.1$ in the AB magnitude

system and the log of the stellar mass in units of $M_{\odot} h^{-2}$. With the exception of the two low-mass ellipticals with smooth morphologies, we find that the low-mass galaxies tend to have the strongest morphological peculiarities and blue colours consistent with star-forming galaxies. The more massive galaxies tend to exhibit green valley colours and smoother morphologies. We note that all of the peculiar ellipticals have masses between $10^{10.5}$ and 10^{11} $M_{\odot} h^{-2}$, above which extremely few blue galaxies lie (e.g. Baldry et al. 2004).

2.2 Observations

Our final sample of 12 plausible merger remnants were observed over three separate runs between 2010 January and 2011 April. We require moderate resolution ($R \simeq 1000$) spatially resolved spectra with wavelength coverage spanning the 4000 Å break and Balmer H δ and H γ absorption indices to obtain SFHs as a function of galactic radius to differentiate between remnants of major mergers from those of other mass assembly mechanisms. The optimal choice for large-field, spatially resolved spectroscopy is an IFU which additionally provides concurrent sky flux measurement to facilitate removal of contaminating sky lines during reduction.

The first observing run was performed between 2010 January 18 and 20 at the 3.5-m Calar Alto observatory in Spain using the Potsdam MultiAperture Spectrophotometer (PMAS; Roth et al. 2005) and the PPAK IFU (Kelz et al. 2006). We used the V1200 grating with first order and forward blaze angle centred on 4263 Å, providing a spectral resolution full width at half-maximum (FWHM) of 2.7 Å, and an observed wavelength range of 3877–4633 Å. The spectra were binned 2×2, giving an instrumental resolution of 0.75 Å pixel^{-1}. The 2.7 arcsec fibres provide a spatial resolution of 1.63 kpc at z=0.03. Three 30 min exposures were taken of each of the three targets, but nyu541044 was shortened by 5 min and nyu835691 by 13 min to reduce background during twilight (see Table 2). The second observing run was performed between 2011 January 31 and February 2 at the 3.5-m WIYN[3] telescope at the Kitt Peak National Observatory in Arizona using the WIYNBench spectrograph and the SparsePak IFU (Bershady et al. 2004). We used the 600 lines mm^{-1} grating with a blaze angle of 10.1° centred on 5500 Å, providing a spectral resolution FWHM of 5 Å, and wavelength range of 3577–6435 Å. The spectra were binned 3×3, giving an instrumental resolution of 1.4 Å pixel^{-1}. The 4.7 arcsec fibres provide a spatial resolution of 2.82 kpc at $z = 0.03$. Five 30 min exposures were taken of each of the eight targets with 10 and 15 min additional exposure to compensate for reduced transparency for nyu598180 and nyu916757, respectively. The third run was performed as part of the Calar Alto Legacy Integral Field Area (CALIFA) survey on 2011 April 11 using the Calar Alto telescope and PMAS with the PPAK IFU. The survey uses a three-pointing dithering with three exposures of 700 s each per dithering with the same V1200 grating set-up used on the previous PMAS observations. In Table 2, we list relevant details from our observing log.

2.3 Data reduction

We use the R3D reduction software (Sánchez 2006) to produce a data cube of wavelength- and flux-calibrated spectra for each

---

[3] The WIYN Observatory is a joint facility of the University of Wisconsin–Madison, Indiana University, the National Optical Astronomy Observatory, and the University of Missouri.
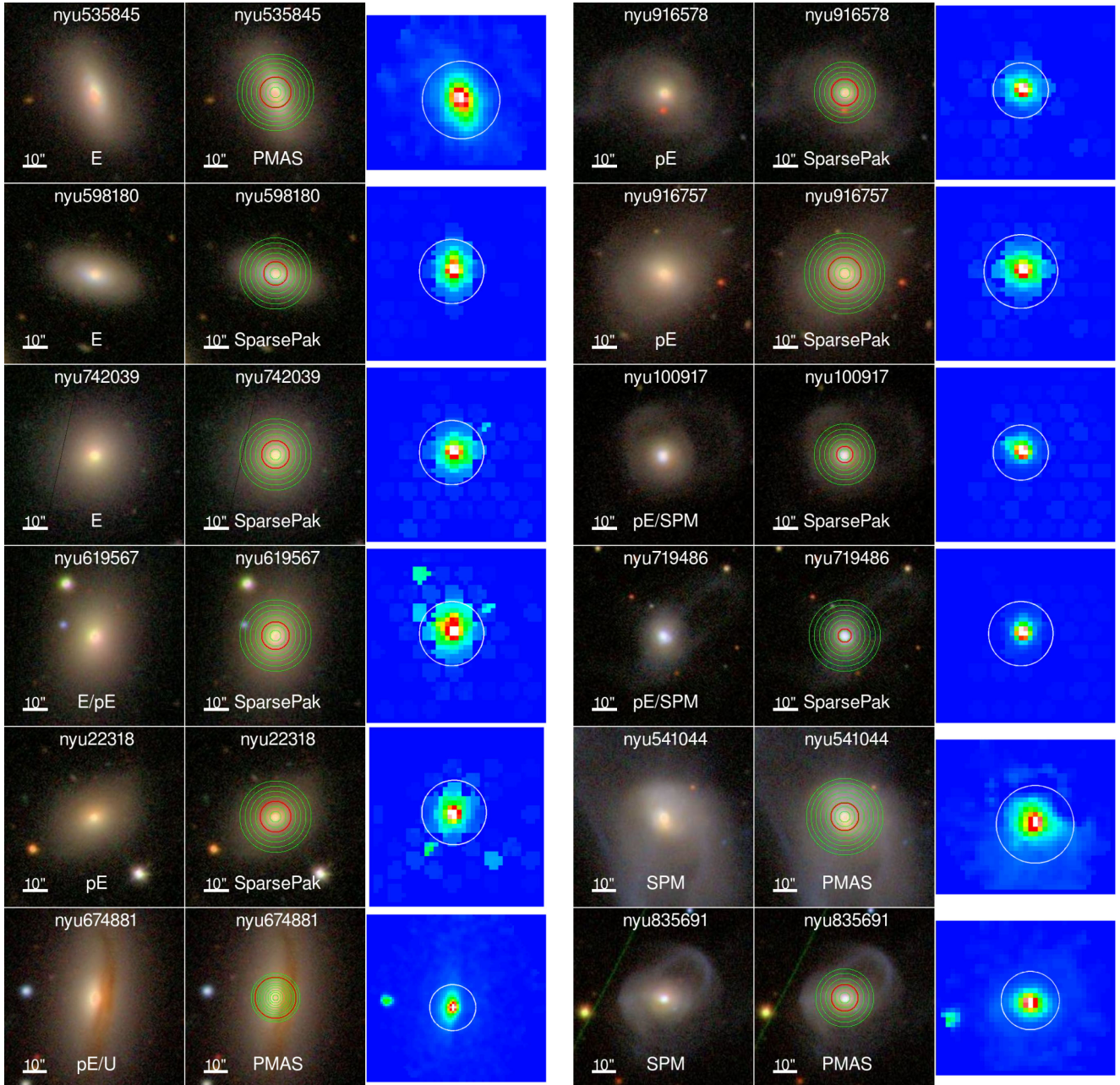
Figure 2. Images of our sample of galaxies. First column: the SDSS thumbnail images scaled to the field of view of the respective spectrograph from which the data were obtained with the morphological classification from M14 shown bottom centre. The white bar indicates 10 arcsec on the sky. Second column: the image from the first column with the binned spectral annuli overlaid and the spectrograph labelled. The red circle represents the half-light radius, R_{50}. Third column: intensity in each spaxel of the data cube at rest frame 4050 Å. The white circle marks the largest annulus seen in the second column. A color version is available in the online journal.

galaxy, which we then use to construct annular spectra for determining the SFHs as a function of galactic radius. The reduction of IFU data starts with the standard procedures for single-slit spectra, namely subtracting the dark current and the bias. We perform cosmic ray rejection using the method of van Dokkum (2001). Because the IFU generates many spectra (82 for SparsePak and 382 for PMAS), the remaining procedures diverge from the normal methods of single-slit reduction. Readers interested in the technical details of IFU data reduction are encouraged to read Sánchez (2006). Here, we provide an outline of our data reduction pipeline.

2.3.1 Reduction of fibre data

(1) Locating spectra on the detector: each exposure from the IFU produces a data frame consisting of the dispersion axis along the horizontal, and N fibre spectra along the vertical (82 for SparsePak, 382 for PMAS). The location of each spectrum along the vertical axis is determined by finding the peak intensity in a sliding window of fixed size oriented vertically and positioned at the centre of the dispersion axis. Once the peaks in the centre column are identified, we next use them as a starting point for finding all of the other spectral pixels for each of the fibre spectra by recursively applying

Table 1. Sample.

Name (1)	$z_{published}$ (2)	R_{50} (3)	c_r (4)	g (5)	M_r (6)	M_* (7)	Classification[a] (8)	Agreement (9)	T_{ppm} (10)	ID (11)
nyu100917	0.027	2.9	3.6	15.10	−21.11	10.24	pE/SPM	50	10	J
nyu22318	0.030	5.9	3.0	14.79	−21.72	10.79	pE	75	7	G
nyu535845	0.014	6.2	3.0	13.99	−20.81	10.24	E	75	5	D
nyu541044	0.020[b]	6.0	3.5	13.55	−22.24	10.61	SPM	75	11	K
nyu598180	0.018	4.4	2.9	14.58	−20.75	10.19	E	75	5	C
nyu619567	0.029	5.2	3.1	14.16	−22.31	10.85	E/pE	50	6	F
nyu674881	0.022	8.3	3.3	13.79	−22.10	10.80	pE/U	50	3	A
nyu719486	0.028	2.4	3.3	15.08	−20.85	10.06	pE/SPM	50	10	I
nyu742039	0.025	5.2	3.1	14.16	−21.90	10.70	E	100	4	B
nyu835691	0.026[c]	5.3	3.4	14.42	−21.41	10.40	SPM	75	11	L
nyu916578	0.029	5.1	3.4	14.85	−21.34	10.51	pE	75	5.5	E
nyu916757	0.028	6.3	3.1	14.19	−22.11	10.77	pE	75	7	H

Note. For each galaxy in our sample, we list (1) the ID provided in the NYU-VAGC from the SDSS DR4, (2) the spectroscopic redshift published in SDSS or NED (objects with a superscript are from NED), (3) the SDSS r-band Petrosian half-light radius in arcseconds, (4) the concentration index given by the ratio of the SDSS r-band Petrosian R_{90} (the radius inside which 90 per cent of the light is contained) and the half-light radius (R_{90}/R_{50}), (5) the SDSS g-band apparent magnitude, (6) the extinction- and k-corrected (to $z = 0$) absolute SDSS r-band magnitude, (7) the stellar mass in units of $\log(M_\odot\,h^{-2})$, (8) morphological classification (see text for details), (9) classifier agreement percentage, (10) the plausible post-merger type parameter (equation 1), and (11) the ID used to refer to each galaxy in figures ordered by increasing T_{ppm}.
[a]All classifications are given where (9) is less than 75 per cent.
[b] Rothberg & Joseph (2006a), [c]Falco et al. (1999).

Table 2. Observing log.

Name (1)	NED name (2)	RA (3)	Dec. (4)	Source (5)	Date (6)	AM (7)	t_{exp} (8)	A_g (9)
nyu100917	MRK 0366	32.8898	13.9171	SparsePak	2011 Jan 31	1.36	9000	1.26
nyu22318	NGC 1149	44.3495	−0.3094	SparsePak	2011 Feb 2	1.33	9000	1.05
nyu535845	UGC 05026	141.6659	45.8472	PMAS	2010 Jan 20	1.08	5400	0.40
nyu541044	NGC 3921	177.7786	55.0788	PMAS	2010 Jan 18	1.05	5100	0.20
nyu598180	CGCG 149−037	127.3750	31.6755	SparsePak	2011 Feb 2	1.05	9600	0.68
nyu619567	IC 0669	166.8190	6.3025	SparsePak	2011 Feb 1	1.15	9000	0.58
nyu674881	NGC 6314	258.1613	23.2701	CALIFA	2011 Apr 5	1.09	6300	0.93
nyu719486	MRK 0385	120.8669	25.1027	SparsePak	2011 Jan 31	1.03	9000	0.44
nyu742039	UGC 06227	167.8640	47.0355	SparsePak	2011 Feb 1	1.51	9000	0.20
nyu835691	UGC 07560	186.7364	48.2770	PMAS	2010 Jan 20	1.02	4600	0.19
nyu916578	CGCG 216−016	189.5908	42.2055	SparsePak	2011 Jan 31	1.11	9000	0.25
nyu916757	NGC 4985	197.0504	41.6763	SparsePak	2011 Jan 31	1.02	9900	0.29

Note. For each galaxy in our sample, we list (1) the ID provided in the NYU-VAGC from the SDSS DR4, (2) the most common associated name in the NASA Extragalactic Database, (3) the right ascension in degrees, (4) the declination in degrees, (5) the IFU on which that data were acquired, (6) the date of observation, (7) the average air mass of all exposures, (8) the total exposure time in seconds, and (9) the SDSS g-band foreground extinction in magnitudes.

the previous procedure to all of the pixels along the dispersion axis of the spectrograph. The fibre spectra are then extracted using the locations of the peak intensities and compiled into a row-stacked spectrum (RSS) such that the x-axis corresponds to the dispersion axis of the spectrograph, and the rows along the y-axis are the fibre spectra listed in IFU order.

(2) Removing distortions and wavelength calibration: the parabolic deflection caused by the inhomogeneous dispersion of light from the pseudo-slit of the IFU fibre bundle as well as fibre-to-fibre distortions which are strongest on the edges of the detector are removed using a two-step process. First, an emission line is chosen from the arc lamp exposure which has strong brightness across all the fibres (i.e. does not suffer from vignetting). The location of this emission line is then traced in each fibre spectrum of the calibration exposure, and the spectra are linearly shifted to a common

dispersion axis such that the selected emission line is located at the same wavelength in each spectrum. A second-order correction using a fourth-order polynomial fit is then used to recentre all of the other emission features. The amount by which each spectral pixel is shifted along the dispersion axis is recorded in the dispersion solution. The observed fibre spectra are then shifted and re-entered in accord with the distortion solution found using the calibration exposure. A standard wavelength calibration is then applied.

(3) Flat-fielding, sky subtraction, and flux calibration: a pseudo-spectrum is constructed for each observed fibre spectrum consisting of the median-combined flux at each wavelength from all of the fibres in the continuum exposure. The fibre spectra are then fibre-flattened by dividing each by this pseudo-spectrum to remove fibre-to-fibre transmission, unevenness in the projection of the fibres through the pseudo-slit, and the inhomogeneous dispersion of light

from the pseudo-slit (see Sánchez 2006 for a thorough discussion of these effects). The effects due to vignetting are then corrected by masking any pixels in the fibre-flatted spectra having less than 70 per cent of the intensity at the same location in the pseudo-spectrum. Next, a new pseudo-spectrum is constructed by linearly interpolating the spectra from the sky fibres (36 for PMAS, 7 for SparsePak) on to a grid the same size as the IFU (382 for PMAS, and 82 for SparsePak), and sky subtraction is performed on each observed fibre spectrum (331 for PMAS, 75 for SparsePak) using these pseudo-spectra. Finally, the observed fibre spectra are flux calibrated using spectrophotometric standard stars acquired during each object's observing run.

(4) Constructing data cubes: the wavelength- and flux-calibrated spectra are converted into a data cube by first populating the pixel space of the first two dimensions of the data cube with discretely sampled points via a standard astrometric transformation with the resulting spaxels (SPAtial piXELS) mapping the fibre spectra on to the sky. Secondly, a smooth, spatially-resolved spectroscopic light profile of each spaxel plane is constructed for each wavelength by blending the light of the discrete points via a two-dimensional Gaussian with a constant circular aperture (see column 3 of Fig. 2). Finally, galactic extinction along the line of sight to each target is corrected using the Charlot and Fall (Charlot & Fall 2000) law combining the g-band extinction values given in the SDSS with table 22 from Stoughton et al. (2002) and equation B1 from Schlegel, Finkbeiner & Davis (1998).

(5) Removing velocity shifts: in this work, we examine large extents of each galaxy's surface where net rotation can contribute substantially to the Doppler shift. Disentangling the component of redshift due to rotation and recessional velocity is a complex task that we do not attempt here. Instead, we fit a combination of one early-type and one late-type spectral energy distribution (SED) from Vazdekis et al. (2010) to the spectrum at each spaxel in the data cube using the FIT3D code (Sánchez et al. 2011) to generate a velocity map containing spatially resolved redshift information over the surface of the galaxy. We input into FIT3D a starting value of the redshift based on a spectroscopic redshift from either SDSS or NED ($z_{\mathrm{published}}$ from Table 1), and the possible range of allowed redshifts given by assumption of a maximum rotation speed of $300\,\mathrm{km\,s^{-1}}$ such that our measured redshifts are in the range $z_{\mathrm{published}} \pm 300\,\mathrm{km\,s^{-1}}/c$. We then use the resulting velocity map to remove the Doppler shift from the spectra. We find excellent agreement between our measured redshifts and those published in the SDSS or NED with a maximum absolute difference of $\sim 30\,\mathrm{km\,s^{-1}}$. The spectra in each data cube are then shifted to a common rest frame such that they all begin at the same wavelength to ensure that co-adding spectra works correctly later.

2.3.2 Constructing azimuthally binned spectra

In this work, we examine the stellar populations over large extents of each galaxy in our sample. There are several methods available for combining IFU spectra to extract spatially resolved stellar populations. For example, the CALIFA collaboration use a Voronoi tessellation (Cappellari & Copin 2003) method to construct local regions with high signal-to-noise (S/N; Cid Fernandes et al. 2013). We utilize a light-weighted azimuthal binning with constant annular width to provide a uniform view of the radial behaviour and concurrently counteract the decreasing S/N at large radii due to lower surface brightness. This method has been recently used to extract detailed Lyman α properties using SSP models (Papaderos et al.

2013) and has been shown to have a nominal effect on the derived stellar population properties (Mast et al. 2014). We use a two-stage process for measuring the S/N pixel^{-1} of our spectra. First, we use the standard method based on counting statistics to ensure only spectra with S/N above the photon-limited regime are considered. Importantly, we measure the S/N pixel^{-1} near the Balmer and 4000 Å break indices used throughout this work. Secondly, we use the technique from Husemann et al. (2013) to account for the cross-correlated noise introduced by co-adding spectra. In this step, we measure the S/N pixel^{-1} in several continuum regions to ensure that our spectra are of generally high quality.

(1) Error estimate using counting statistics: starting with the azimuthally binned spectra, we utilize the signal (in counts) and the noise (in counts) at each wavelength to calculate the S/N pixel^{-1}. To do this, we first construct an RSS of the estimated Poisson noise via the standard formula $noise = \sqrt{source + background + readout^2}$, where the source and background are the raw (i.e. not flux-calibrated) spectrum and sky counts, respectively, and *readout* is the readout noise from the detector. We then convert the raw spectra and the noise RSS into data cubes following the procedure outlined in point (iv) of Section 2.3.1 and apply the velocity shift corrections discussed previously. Finally, for each annulus we construct the azimuthal sum of the spaxels in the raw spectra data cube and the quadrature sum of the corresponding spaxels from the noise data cube to compute the S/N pixel^{-1} in the wavelength regions around the $D_{\mathrm{n}}(4000)$, H γ, and H δ indices. Because absorption features have intrinsically less S/N pixel^{-1} than equivalent continuum measurements, we retain annular spectra with a minimum S/N pixel^{-1} of 5 in each region around the three indices.

(2) Full spectral fitting: our analysis centres on the equivalent width measurements of the Balmer H γ and H δ indices. To measure these accurately, we must first determine the amount of nebular contamination present in our spectra. To measure this, we use the full-spectral fitting code FIT3D (Sánchez et al. 2011) and a catalogue of thirty SEDs to find a combination which reproduces our spectra in the minimum chi-squared sense. We use the single stellar population (SSP) SEDs generated from the MILES library using the code from Vazdekis et al. (2010) with metallicities of 2, 20, and 100 per cent solar each spanning a range of 10 ages from $\sim 70\,\mathrm{Myr}$ to $\sim 14\,\mathrm{Gyr}$. We first fit our spectra with all of the Balmer and forbidden oxygen emission lines masked. The total velocity dispersion (i.e. stellar and instrumental) and internal dust extinction[4] are treated as free parameters and fit in the minimum chi-squared sense. The generated continuum fits are then subtracted from the spectra, and the emission lines are fit.

We fit a single Gaussian to each emission line individually with the line centre, FWHM, and peak amplitude treated as free parameters. We attempt to fit all of the Balmer and forbidden oxygen lines masked during the continuum fitting, but require that the peak of each emission fit be greater than 1σ of the flux contained in a window of 20 around the known line centre to prevent fitting noise. We reject residual sky lines and any remaining cosmic rays using a windowed boxcar filter to replace the flux exceeding 3σ of the flux in the window with the average of the flux in the window. The emission fits are then subtracted from the original spectra, and the FIT3D continuum fits are performed again with none of the emission lines masked. This new continuum fit is then used to perform the emission line fitting and clipping again to produce a set of emission-free spectra.

---

[4] Foreground extinction has already been removed at this point.

(3) Constructing variance maps: During the binning process spatially coherent, but physically independent spectra are co-added to increase the S/N per pixel. By combining independent spectra, an artificial noise is introduced into the final spectrum we wish to use to make our measurements. To trace this spatially correlated noise, we use the methods of Husemann et al. (2013) to construct a *variance map* to estimate the correlated noise at each wavelength using the SED fits to our emission-subtracted spectra calculated above. The variance map is simply the median-smoothed residuals from the full spectral fitting. Under the assumption that our statistical method provides the 'true' measure of the noise in the spectra, the variance map is considered to be a direct measure of the correlated noise introduced during the azimuthal binning. We then use the variance map as the final measure of the error to recompute the S/N pixel^{-1}. For this final step, we use the three regions (4040,4060 Å, 4150,4200 Å, 4380,4430 Å) which measure the S/N pixel^{-1} in the continuum (rather than in the indices) where there is less change in model-data discrepancies to improve our index measurements. Because we are measuring only continuum regions here, we require a greater minimum S/N pixel^{-1} than was considered when constructing error estimates using counting statistics where absorption features were used to measure the S/N pixel^{-1}. Only spectra with S/N pixel^{-1} > 10 are retained for further analysis. We show our sample with the annuli overlaid on the SDSS images and the intensity map from the data cube at 4050 Å in Fig. 2 and the final set of annular spectra for each galaxy in Fig. C1.

2.3.3 Index measurements

Starting with the set of fully reduced and calibrated emission-subtracted annular spectra in Appendix C, we measure the H δ_A and H γ_A Lick indices and the narrow-band 4000 Å break as a function of galactic radius. To calculate the strength of each index, we first define three passbands around each index's line centre: the blue continuum, the central region, and the red continuum. The passbands for the Lick H δ_A and H γ_A indices from Worthey & Ottaviani (1997) and the narrow-band 4000 Å break (hereafter referred to as $D_n(4000)$) from Balogh et al. (1999) are shown in Fig. 3. To reduce random errors in the outermost annuli of our galaxies, we use the average Balmer index ⟨H δ_A, H γ_A⟩ ≡ (H δ_A + H γ_A) /2 from Sánchez-Blázquez, Gorgas & Cardiel (2006).

In general, differences in $D_n(4000)$ correspond to differences in the ages of stellar populations on the order of several Gyr, and differences in Balmer strength correspond to differing fractions of A stars. We show our index measurements as a function of galactic radius organized by morphological classification in Fig. 4. Examining the radial trends of the indices, we find that strongly disturbed galaxies (visually classified as SPM or pE/SPM) exhibit flat or decreasing Balmer absorption at increasing radii with generally increasing $D_n(4000)$ values with increasing galactic radius – indicating that the youngest stellar populations are in the galaxies' cores. For the modestly disturbed galaxies (pE) and two of the smooth ellipticals (E) nyu742039 and nyu619567, we find generally decreasing $D_n(4000)$ and increasing Balmer values at increasing radii consistent with their oldest stellar populations residing in their cores. We note that most of the Balmer radial indices are negative and hence not indicative of stellar populations containing a large fraction of A stars. However, there are two exceptions: nyu674881 and nyu916578 have positive Balmer absorption values at their largest radii. The final two smooth ellipticals (E) nyu598180 and nyu535845 are distinct in that they have positive Balmer absorption values at nearly all radii and
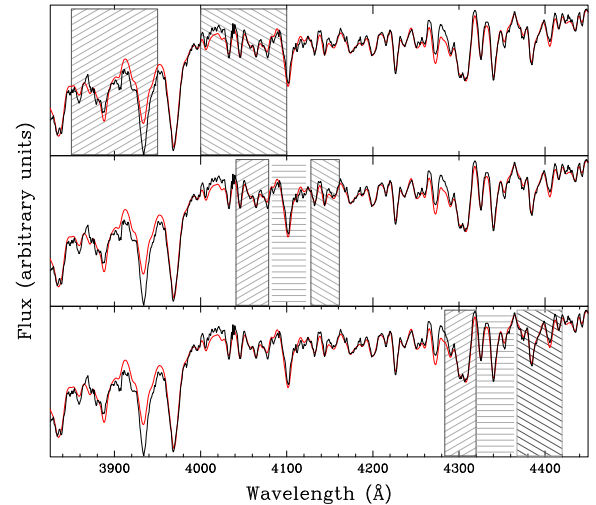

Figure 3. Definitions of the blue continuum (upwards-hatched), central (horizontal-hatched), and red continuum (downwards-hatched) passbands for the $D_n(4000)$ (top), H δ_A (centre), and H γ_A (bottom) indices from an example galaxy. The measured spectrum is shown in black, and the continuum fit is shown in red. Note that the $D_n(4000)$ index definition does not include a central continuum. The *y*-axis shows the flux arbitrarily scaled to show detail, and the *x*-axis shows the rest-frame wavelengths. A color version is available in the online journal.

small $D_n(4000)$ values near the range of values exhibited by the SPM galaxies. From Fig. 2, we see that these two galaxies possess blue circumnuclear rings consistent with recent star formation. As discussed in Section 2.1, our choice to include galaxies with interesting morphological details such as the blue rings seen here has paid dividends in that we find there need not be a direct correlation between a galaxy's general morphology and its *recent* SFH.

3 MODELLING STAR FORMATION HISTORIES

In this work, we seek to test if the modern merger hypothesis can account for the assembly of our sample of plausible new ellipticals with unusually blue optical colours. Specifically, we use the prediction that the blue-to-red migration leaves behind a tell-tale signature via the presence of a strong, centrally-concentrated burst of star formation in the merger remnant. This signature can be detected in our sample of plausible new ellipticals by comparing the measured Balmer and $D_n(4000)$ indices (see Section 2.3.3) to a suite of specially constructed models.

We use the iSEDFit tool from the IMPRO code package[5] to construct a suite of theoretical SEDs covering many different SFHs (see appendix A of Moustakas et al. 2013, for details). We begin construction by characterizing the star formation rate (SFR) as a function of time for an arbitrary stellar population using a simple, exponentially declining SFR such that SFR$(t) \propto e^{-t/\tau}$ where τ is the characteristic time. We then allow for two possible evolution paths: one in which the galaxy continuously forms stars throughout its lifetime and a second in which the galaxy experiences a burst of star formation superimposed atop a continuously declining SFH (see Appendix A for details).

The continuous models begin with a large burst of star formation at $t = 0$ and evolve for ∼15 Gyr with a continuous, exponentially

---

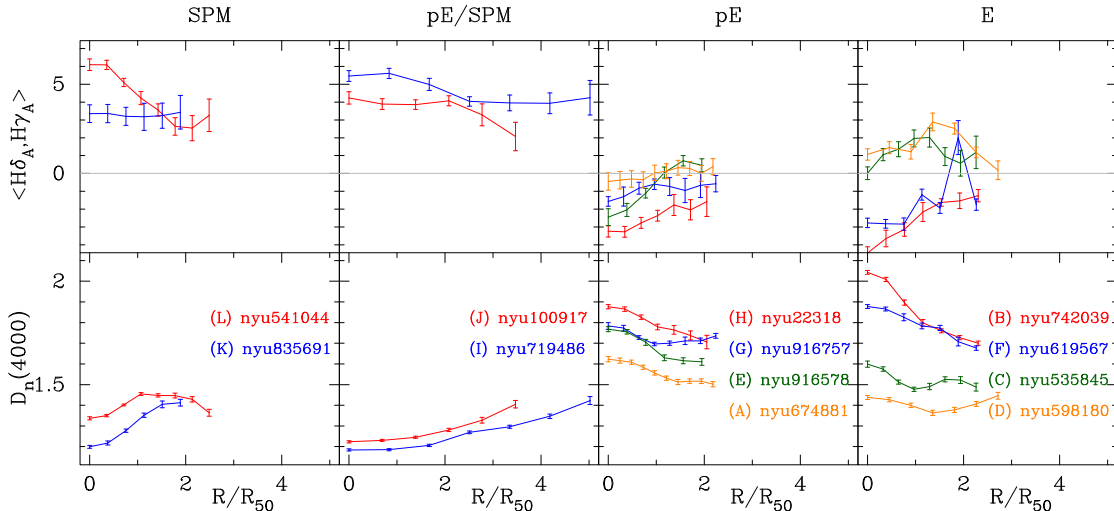[5] https://github.com/moustakas/impro

Figure 4. Average stellar Balmer absorption indices, $\langle H\delta_A, H\gamma_A \rangle \equiv (H\delta_A + H\gamma_A)/2$, and the 4000-Å break strength, $D_n(4000)$, as a function of the SDSS Petrosian *r*-band half-light radius (R_{50}) organized by morphological classification. Colours represent indices from the same galaxy in a single column. A color version is available in the online journal.

declining SFR. For these models, we allow a range of e-folding times from 7 Gyr representative of normal star-forming late-type galaxies to 0.5 Gyr signifying a quenching of star formation. The burst models start with the same large burst at $t = 0$ as in the continuous models but add an additional burst of star formation generating between 1 and 25 per cent of the total mass of the galaxy atop the exponentially declining star formation when the galaxy is $\sim$12 Gyr old. We use e-folding times from 25 Myr to 1 Gyr representative of strongly- and weakly truncated bursts of star formation, respectively. These burst models reflect the scenario in which our plausible new ellipticals formed from a *recent* ($z = 0.12$) gas-rich merger and evolved to today with varying degrees of quenching over a period of evolution on the order of the dynamical merger time ($\sim$1 Gyr; Lotz et al. 2008). To produce the final model spectra, we convolve the constructed SFHs with a set of SSP SEDs from Bruzual & Charlot (2003) spanning their full range of metallicities from 0.005 to 2.5 $Z_\odot$ with the Chabrier IMF.

3.1 Index plane

We use the established technique of comparing the 4000-Å break strength with the Balmer Lick indices $H\gamma_A$ and $H\delta_A$ to qualitatively distinguish between galaxies that have a simple, continuous SFH from those that have undergone a burst of star formation within the last $\sim$1 Gyr (Kauffmann et al. 2003a, K03). Fig. 5 shows the indices measured from our continuous models (blue) and our burst models (green and red) in the Balmer–$D_n(4000)$ plane. We note that though there are parts of parameter space that can clearly only be reached by models with bursts, the burst models substantially overlap the regions of parameter space covered by the suite of continuous models; a result of the age-burst degeneracy. The locus of points extending along any continuous model track can be explained by a range of continuous SFHs of different e-folding times and luminosity weighted ages at fixed metallicity. As shown by K03, this locus is not as sensitive to metallicity as the indices themselves and acts as a simple diagnostic allowing us to qualitatively separate galaxies undergoing continuous star formation from those which have undergone a burst of star formation in the last 1–2 Gyr in which at least 5 per cent of their mass was formed.

To simplify our analysis, we choose our fiducial burst and continuous models (blue, red, and green model tracks in Fig. 5) to have solar metallicity. We choose solar metallicity for three reasons: (1) interpretation of the age and chemical composition of composite stellar populations determined with line-strength indices depends upon the chemical composition of the underlying 'old' stellar populations (Serra & Trager 2007), (2) SDSS galaxies in our mass range have *unresolved* metallicities near solar (Gallazzi et al. 2005), and (3) local elliptical galaxies have shallow gradients in their SSP-equivalent chemical compositions (Trager et al. 2000a). We note, however, that within both the continuous and burst SFH models, metallicity gradients can plausibly mimic age gradients, and caution against overinterpreting the model plane.

Points in the plane which lie above the continuous models (i.e. have a more positive Balmer absorption index at a fixed $D_n(4000)$) can be explained by a range of burst SFHs of different e-folding times, luminosity-weighted ages at fixed metallicity, and fraction of new stars formed during the added burst. Because of this degeneracy we do not try to precisely constrain model parameters such as e-folding times, etc. Yet, by comparing the data to our chosen models sampling the extrema of reasonable e-folding times and luminosity-weighted ages, we can draw several qualitative conclusions. To do this, we divide the Balmer–$D_n(4000)$ parameter space into four regions by combining the known properties of the constructed models with the regions of the Balmer–$D_n(4000)$ plane where K03 found 95 per cent of their simulated galaxies had high probabilities of forming either at least 5 per cent or exactly none of their stars in a burst within the last 2 Gyr (see fig. 6 in K03 for details).

The first region (region 1) in the model plane contains the radial indices with $D_n(4000) \lesssim 1.35$ that lie on or below the continuous SFH models where typical late-type star-forming galaxies are found. We note that points lying along the burst models having ages $\lesssim$200 Myr also reside in this region. This is an example of the well-known age-burst degeneracy wherein a large burst of star formation occurring long ago (here, the continuous model) mimics the behaviour of a recent, smaller burst. The second region (region 2) contains the range $1.35 \lesssim D_n(4000) \lesssim 1.6$ and lies on or below the continuous SFH model with a short e-folding time
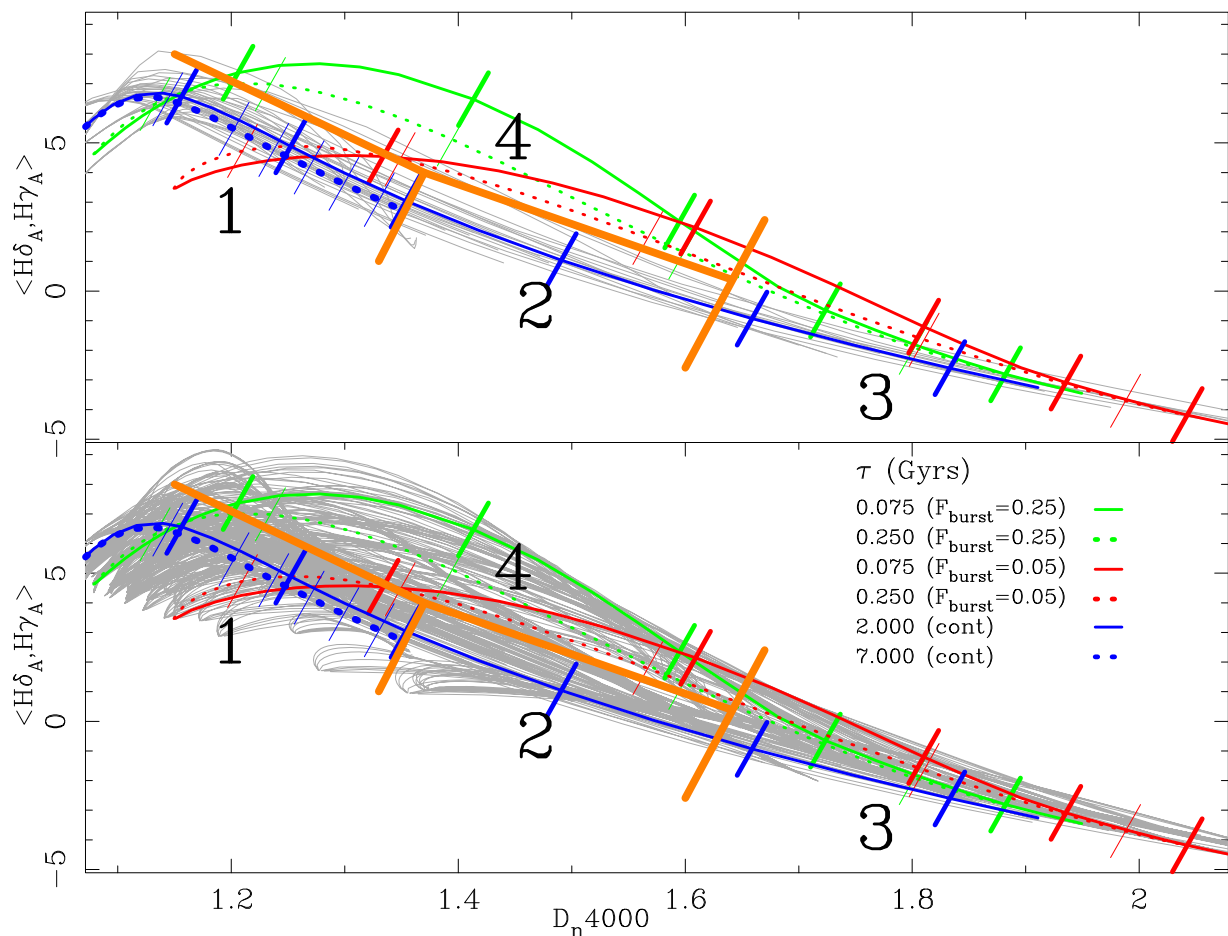
Figure 5. The stellar Balmer absorption versus 4000-Å break strength model plane showing two continuous SFH models (blue), two burst models in which 25 per cent of the total galaxy mass was formed in a single burst (green), and two burst models with a 5 per cent burst fraction (red). Tick marks denote ages along the model lines. For the continuous models, the ages are 1, 3, 5, 7, 9, and 11 Gyr. For the burst models, the ages (i.e. time since the burst) are 0.2, 0.5, 0.9, 1.5, and 2.5 Gyr. The four qualitative regions from the text are labelled and orange lines mark their approximate boundaries. The full suite of continuous (top) and burst models (bottom) covering their respective full parameter spaces are shown in light grey. A color version is available in the online journal.

($\tau = 2$ Gyr, solid blue lines). In this region, we find galaxies having luminosity-weighted ages between ~5 and 9 Gyr, but note that adding a few per cent of new stars by mass atop an older population can mimic these ages.

The third region (region 3) contains the radial indices with $D_n(4000) \gtrsim 1.6$ and lying in the region where the continuous and burst models overlap. At fixed $D_n(4000)$, measurements in this region have Balmer absorption indices which span from the continuous SFHs consistent with old stellar populations in quiescent ETGs to the 5 per cent burst models with luminosity-weighted ages $\gtrsim 1$ Gyr. Finally, the fourth region (region 4) spans $D_n(4000) \lesssim 1.6$ and is bracketed above the continuous SFH models. This region is described by K03 as containing galaxies with a high confidence of having undergone a burst of star formation in the last ~2 Gyr. The individual Balmer–$D_n(4000)$ planes with the radial indices for each galaxy in our sample are shown in Fig. B1.

3.2 Comparing models and data

In Fig. 6, we overlay all of our radial index measurements from all galaxies in our sample atop our full suite of models and find two notable conclusions. First, our measured indices span nearly the entire

model space indicating that our sample of galaxies possesses a wide range of SFHs (although radial information is not recoverable here). Secondly, our chosen model space completely covers our measured indices.[6] This indicates that our choice of model parameters is congruent with the local population of plausible new ellipticals. We note that many of the points that lie in the fourth region of the plane (i.e. bracketed above the continuous models – blue) reside below the burst models with burst fractions of 5 per cent (red) and are more consistent with burst models with smaller burst fractions (e.g. ~1 per cent). We defer to future work to recover detailed SFHs for individual data points.

In Fig. 7, we show the Balmer and $D_n(4000)$ radial indices for each of our galaxies organized by the region in which most of the indices lie (see Appendix B for individual Balmer/$D_n(4000)$ planes). Galaxies with radial indices in two different regions of the plane (e.g. nyu916578) are assigned to the region where their central annuli lie. Comparing with Fig. 4, we see that the first and fourth regions of the Balmer–$D_n(4000)$ plane contain the most morphologically disturbed galaxies ($T_{\rm ppm} \geq 10$) with flat or slightly decreasing

---

[6] The one outlier near $D_n(4000) \simeq 1.7$ is shown in Section 4.3 to likely be a measurement error.
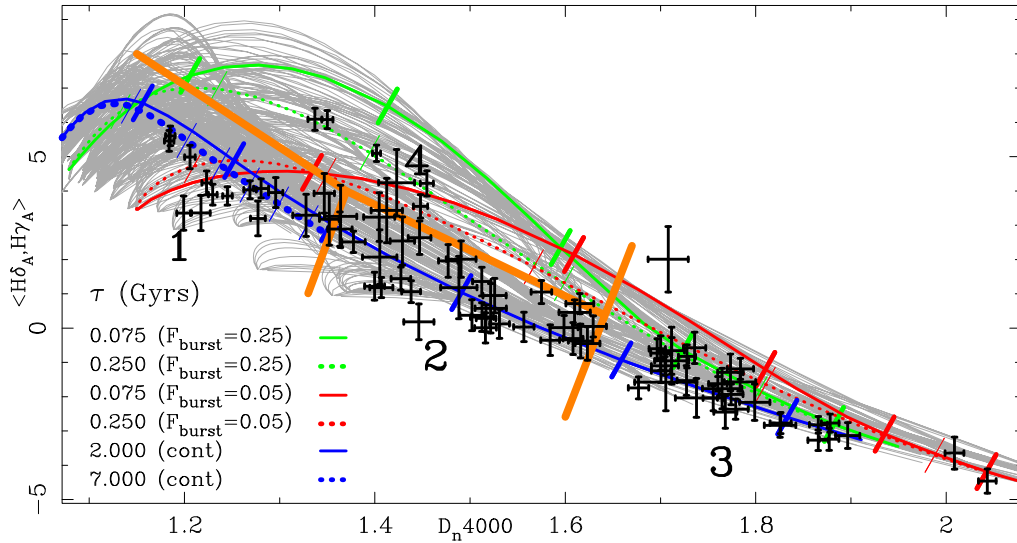
Figure 6. The stellar Balmer absorption versus 4000-Å break strength model plane as from Fig. 5 with our measured radial indices and their errors for all radii (see Fig. B1) of our entire sample are shown in black. The complete suite of continuous and burst models are shown in grey. The four qualitative regions from the text are labelled and orange lines mark their approximate boundaries. A color version is available in the online journal.
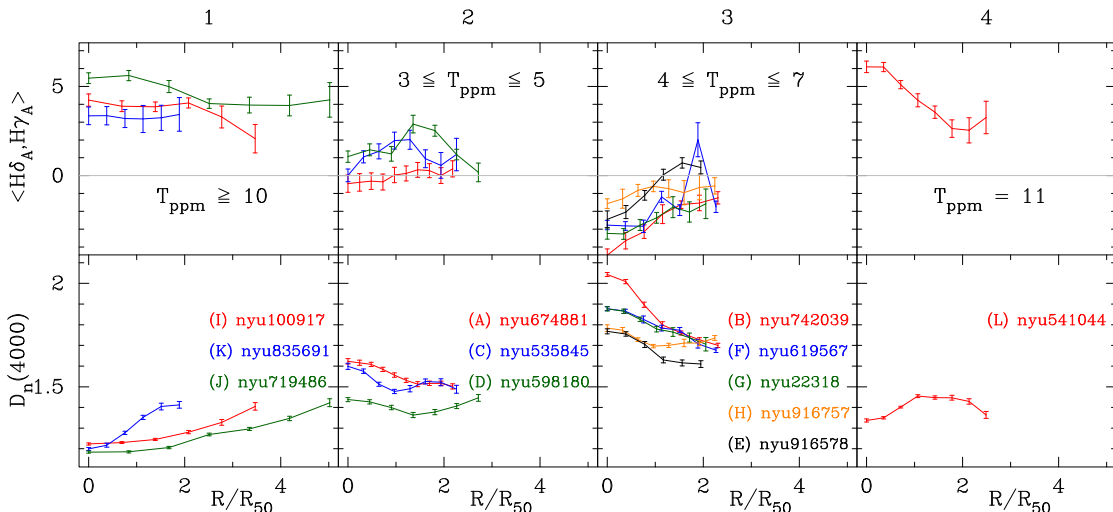

Figure 7. The average stellar Balmer absorption indices, $\langle H\delta_A, H\gamma_A \rangle \equiv (H\delta_A + H\gamma_A)/2$, and the 4000-Å break strength, $D_n(4000)$, at each annulus shown as a fraction of the SDSS Petrosian r-band half-light radius (R_{50}) for each galaxy organized by location in the Balmer–$D_n 4000$ plane (see Appendix B). Colours represent indices from the same galaxy in a single column. The range of T_{ppm} values from Table 1 are shown for the galaxies contained in each region of the plane where larger values indicate stronger morphological disturbances. A color version is available in the online journal.

Balmer index gradients and generally increasing $D_n(4000)$ indices at large radii. With burst-like SFHs and very young stellar ages in their cores, these galaxies are likely candidates of recent gas-rich major mergers. If the dynamical disturbance is due to merging activity as predicted by the modern merger hypothesis, the dichotomy of regions in the plane where strongly disturbed galaxies lie indicates that not all mergers result in starbursts – consistent with predictions from simulations (e.g. Cox et al. 2008). Galaxies in region 2 have smooth elliptical morphologies ($T_{ppm} \leq 5$) and SFHs consistent with weak, but ongoing, star formation. Galaxies in region 3 have steep positive Balmer index gradients and steep negative $D_n(4000)$ gradients indicative of very old stellar ages in their central regions, implying they are the least likely to be remnants of recent gas-rich major mergers. Surprisingly, these galaxies exhibit a variety of elliptical morphologies ($4 \leq T_{ppm} \leq 7$) including some with clear

signs of interaction (e.g. nyu916578), but possess stellar ages much older than those found in the smooth ellipticals in region 2.

4 DISSECTING ASSEMBLY HISTORIES

A key prediction of the modern merger hypothesis is the presence of a strong, centrally concentrated burst of star formation in the merger remnant. We anticipate this inside-out growth produces a distinct radial SFH which we can use to qualitatively differentiate plausible remnants of major mergers from galaxies undergoing other mass assembly mechanisms. Combining our spectroscopic radial index measurements with our qualitatively defined regions of the Balmer–$D_n(4000)$ plane (see Section 3.1), we ask the question whether each galaxy in our sample is consistent with the predictions of the modern
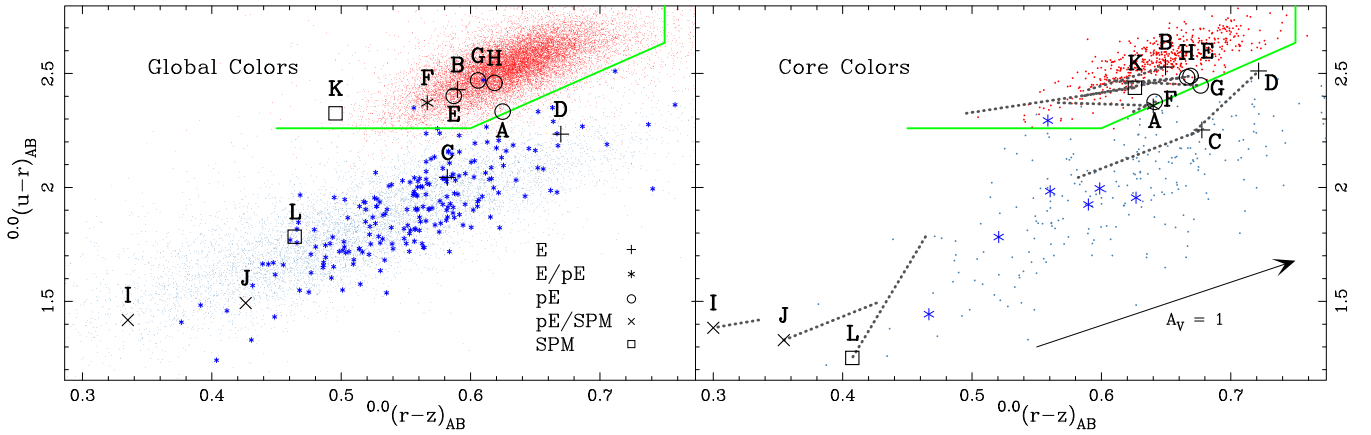
Figure 8. (Left) Global $(u-r)$ and $(r-z)$ colours and (right) core colours from the SDSS k-corrected to redshift zero in the AB magnitude system overplotted on the quiescent (red) and star-forming (blue) control samples described in Section 4. Core colours are shown only for galaxies with $z \leq 0.03$ to match the redshift of our sample and minimize aperture effects. The dotted lines in the figure on the right connect the core colours with the corresponding global colours for each galaxy. Symbols represent visual classifications from M14. The empirical boundary from Holden et al. (2012, green) robustly separates the star-forming and non-star-forming galaxies with star-forming galaxies below the line. The complete sample of star-forming elliptical galaxies from M14 is shown in blue asterisks. Letter labels are from Table 1. A color version is available in the online journal.

merger hypothesis; i.e. having preferentially younger stars in its core formed in a recent burst.

Additionally, we anticipate central star formation to alter the galaxy's optical colours such that it either preferentially contains more blue light in its core or its core colours are reddened consistent with the presence of merger-induced dust. We therefore examine the distribution of global colours using the SDSS $(u-r)$ and $(r-z)$ model magnitudes (Fig. 8, left-hand panel) and core colours using the SDSS fibre magnitudes (right-hand panel); both are k-corrected to redshift zero in the AB magnitude system. For comparison, we show the control samples from M14 of red, spectroscopically quiescent ETGs and blue, star-forming LTGs from the SDSS with the same mass and redshift range as our sample. For the core colours, we show only those galaxies with $z \leq 0.03$ to match the redshift range of our sample and limit the spatial bias of the SDSS fibre aperture.[7] In both panels, we show the empirical boundary from Holden et al. (2012) which robustly separates star-forming red (dusty) galaxies from non-star-forming (old) galaxies. M14 show that 92 per cent of all spectroscopically quiescent galaxies from their complete sample lie above this line and 97 per cent of BPT star-formers lie below it. Additionally, we overlay the sample of spectroscopically confirmed star-forming ellipticals from the M14 sample as blue asterisks.

In Fig. 9, we provide quantitative colour gradients in the SDSS $(u-r)$ and $(r-z)$ colour–colour plane for our galaxies and the subset of the comparison samples shown in Fig. 8 with $z \leq 0.03$. The colour gradients are defined by $\Delta C = C_{outer} - C_{core}$ where C is one of $(u-r)$ or $(r-z)$. The outer colour C_{outer} is derived by converting the respective SDSS model magnitudes into flux, subtracting the flux from the SDSS fibre magnitudes, and converting to a colour. We note that the colour gradients computed here are not the same as the tracks shown in the right-hand panel of Fig. 8 which show the relative position of each galaxy in the colour–colour plane according to its core and global colours.
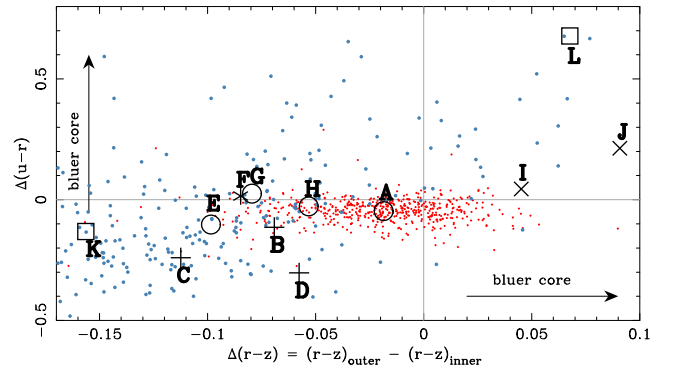

Figure 9. The SDSS model $(u-r)$ and $(r-z)$ colour gradients for massive ($\log M_* \geq 10$), nearby ($z \leq 0.03$) galaxies. We show the spectroscopically quiescent ETG (red) and blue star-forming LTG (blue) control groups from Fig. 8. Our sample of massive blue ellipticals are shown using their respective morphological symbols and labels as in Fig. 1. Each 'blue core' vector points in the direction of its respective colour gradient having a bluer core colour. A color version is available in the online journal.

4.1 Are starbursts always concurrent with major mergers?

Examining Figs 4 and 7, we find that only one (nyu541044) of the four galaxies visually classified as SPM or pE/SPM (i.e. $T_{ppm} \geq 10$) has radial indices in region 4. In particular, Fig. 10 shows its central indices are consistent with our burst models in which ≥ 15 per cent of its stars formed in a recent burst and have luminosity-weighted ages ≤ 1 Gyr (measured relative to the start of the burst). Surprisingly, this galaxy's global and core optical colours both lie in the non-star-forming region of colour–colour space as determined by the Holden boundary (Fig. 8). However, its colour gradients lie outside the locus of local ETGs and are more steeply negative (i.e. redder cores) than $\sim$80 per cent of the local star-forming LTGs (Fig. 9). This combination of clear burst signature and quiescent core colours is consistent with post-starburst galaxies which are characterized as having recently undergone a large burst of star formation quickly followed by strong quenching.

Indeed, previous spectroscopic study of this galaxy by Schweizer (1996) found this to be the case; although we find a slightly higher

---

[7] For the redshift range of our targets, the 3 arcsec SDSS fibre aperture corresponds to between 0.86 and 1.8 kpc.
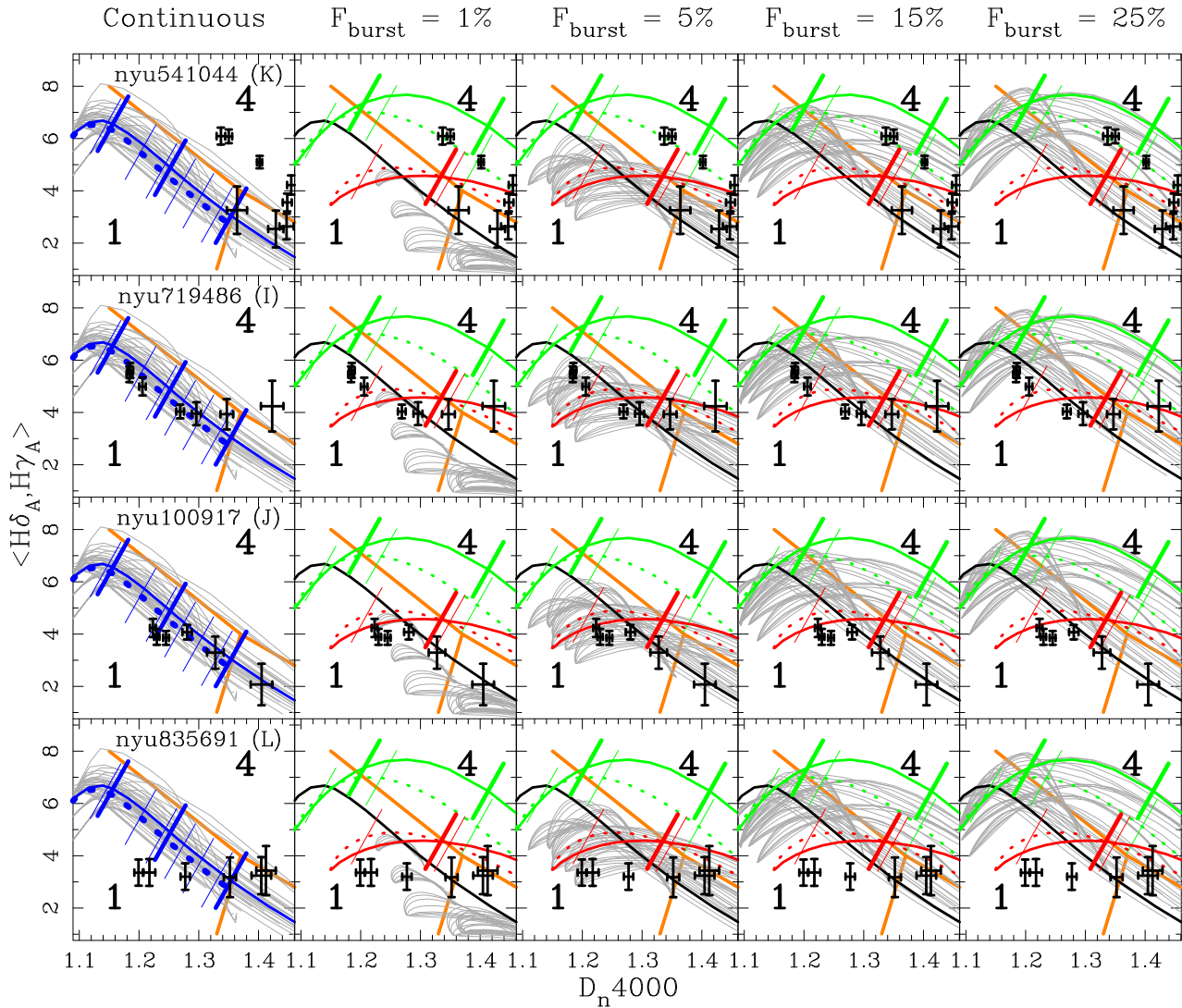
Figure 10. Zoom-in of regions 1 and 4 of the Balmer–$D_n(4000)$. Column 1 shows the full suite of continuous models in grey and highlights the two fiducial models used throughout this work in blue. Columns 2–5 show the full suite of burst models in grey with the fraction of stellar mass formed during the burst increasing to the right. The two sets of fiducial burst models used throughout this work are shown in red (5 per cent burst) and green (25 per cent burst). The fiducial continuous model with an e-folding time of 7 Gyr is shown in solid dark grey alongside the burst models as a guide. Each row shows the radial index measurements corresponding to the galaxy listed in the first column. A color version is available in the online journal.

fraction of new stars formed in the burst (≥ 15 per cent compared to their ~10 per cent) likely attributable to the more modern stellar template libraries used in constructing our burst models. Galaxies with post-starburst signatures are also referred to as E+A galaxies due to their spectra appearing as a superposition of an elliptical galaxy (i.e. very little nebular emission) and that of A-type stars (Dressler & Gunn 1983). From Fig. C1, we see the presence of both an elliptical-like spectrum as well as the Balmer absorption features in our observed spectra for this galaxy. Additionally, the lack of dust signatures in the optical colours of this galaxy (Fig. 8) is consistent with local E+A galaxies being quenched post-starbursts rather than starbursts with dust-obscured nebular emission (Goto 2004).

The characteristics of E+A galaxies have been shown to be consistent with the transformation from a gas-rich, star-forming disc galaxy to a gas-poor, quiescent, pressure-supported spheroidal galaxy (Norton et al. 2001), and are hypothesized to come from gas-rich major mergers (Cox et al. 2008; Goto et al. 2008; Wild et al. 2009; Pracy et al. 2012). The molecular gas density profile

of this galaxy (Hibbard & Yun 1999) is consistent with the centrally concentrated gas deposition predicted in simulations of major mergers (e.g. Barnes & Hernquist 1991). The qualitative luminosity-weighted ages we find in its central annuli are consistent with the lifetime of the short (~0.1–0.3 Gyr) E+A signatures seen in simulations (Snyder et al. 2011). Without further spectroscopic measurements, we are unable to draw any conclusions regarding the role of an AGN as the truncation mechanism as predicted by the modern merger hypothesis. Clearly, though, the preponderance of evidence indicates that this galaxy is a strong candidate of being a remnant of a recent, gas-rich major merger.

The remaining three galaxies with $T_{\mathrm{ppm}} \geq 10$ have star-forming global colours with bluer core colours (Fig. 8) and steeper positive (i.e. bluer core) colour gradients than ~96 per cent of the local population of star-forming LTGs (Fig. 9). These strongly disturbed galaxies have generally larger Balmer absorption values and smaller 4000-Å break strengths than all of the other morphology types (Fig. 4), and specifically have their largest Balmer and smallest

$D_n(4000)$ values in their centres – consistent with young, centrally concentrated stellar populations. These characteristics match the core star formation coincident with strong morphological disturbances predicted by the modern merger hypothesis and are consistent with these galaxies forming via gas-rich major mergers. Unlike nyu541044, however, these galaxies lack any indication of post-starburst signatures. Rather, they lie in region 1 (Fig. 7) of the Balmer–$D_n(4000)$ plane and exhibit a dichotomy of plausible SFHs from long-lived continuous star formation to a small, recent burst of star formation. As noted in Section 3.1, the overlap between the continuous and burst models in this region is a consequence of the well-known age-burst degeneracy. The intricacies of this effect are outside the scope of this work, yet we can constrain the plausible formation scenarios by carefully examining region 1 over our suite of models.

In Fig. 10, we show a zoom-in of the Balmer–$D_n(4000)$ plane covering regions 1 and 4 with varying configurations of the parameter space from our models. Of the three galaxies which lie in region 1, only nyu835691 exhibits central indices which are *inconsistent* with the continuous models. For the two galaxies with central annuli consistent with the fiducial continuous models, we note that these models exhibit luminosity-weighted ages in region 1 ranging between 1–11 Gyr depending on e-folding time. However, such large ages are in conflict with the predicted lifetimes of the tidal features seen in these galaxies (see below). Although our observations do not conclusively exclude the continuous models, we note that they are only plausible for these two galaxies and do not consider them further. Examining the burst models in columns 2–5, we see that all three galaxies are generally inconsistent with the extreme models having burst fractions of 1 and 25 per cent, respectively. For the models with moderate burst fraction, we see that the radial indices of all three galaxies lie along the model tracks with $F_{burst} = 5$ per cent (consistent with the findings of K03 for this region), but only nyu719486 has *central* indices along the model tracks with the 15 per cent burst fraction.

Focusing on the burst models with $F_{burst} = 5$ per cent, we find very young luminosity-weighted ages ($\lesssim 200$ Myr, measured relative to the time of the burst) over all metallicities and e-folding times. Given that the burst models were constructed with the burst (and thus the merger) occurring at $z = 0.12$ and our galaxies have redshifts of $z \simeq 0.03$, this leaves an intermission of ~1 Gyr between coalescence of the merger progenitors and our observations of these galaxies (assuming our chosen model is correct). This period is consistent with the lifetimes of the strong tidal signatures and asymmetries seen in these galaxies as well as in simulations of gas-rich major mergers (Lotz et al. 2008).

The lack of clear signatures of a large burst of star formation in three of the four SPM or pE/SPM (i.e. $T_{ppm} \geq 10$) galaxies in our sample is consistent with previous studies of blue spheroids (e.g. Tojeiro et al. 2013) and actively star-forming local ellipticals (Fukugita et al. 2004) which were shown to have SFHs similar to the long-lived star formation seen in local star-forming LTGs. This indicates that not all plausible major merger remnants undergo an intense burst of star formation. Indeed, this dichotomy is also seen in simulations of gas-rich major mergers which show that the strength and duration of merger-induced starburst activity is likely dependent upon the gas mass fraction and mass ratios of the progenitor discs (Cox et al. 2008) as well as orbital parameters at fixed masses (Snyder et al. 2011). We therefore find that they are likely candidates of being remnants of recent, gas-rich major mergers.

4.2 Dusty ellipticals temporarily removed from the red sequence?

As shown in Fig. 7, galaxies with radial indices lying principally in region 2 of the Balmer–$D_n(4000)$ plane exhibit relatively flat gradients in $D_n(4000)$ ($\Delta D_n(4000) \simeq 0.1$) but non-uniform gradients in Balmer absorption that peak at radii $>1R_e$. The flat gradients in $D_n(4000)$ with variable Balmer absorption are indicative of a changing fraction of young (<1 Gyr) stars atop a uniform, older population. Such a 'frosting' of low-level star formation (Trager et al. 2000b; Yi et al. 2005; Kaviraj et al. 2009; Salim & Rich 2010) may add only 1–2 per cent to a galaxy's mass, but has enough hot O and B stars to produce a brief blue colour migrating these ellipticals temporarily bluewards off of the red sequence into the green valley (Cortese & Hughes 2009; Thilker et al. 2010). Overall, these galaxies have smooth morphologies (E), but nyu674881 is labelled pE owing to its large, circumgalactic dust ring (Fig. 2).

Examining their colours in Fig. 8, we find the two ellipticals ($T_{ppm} = 5$) have global colours which lie in the region of the colour–colour plane occupied by star-forming LTGs as well as the spectroscopically confirmed star-forming ellipticals from M14. Their core colours track upwards along the dust-reddening vector away from the star-forming ellipticals towards redder colours; suggesting the presence of central dust obscuration. Their colour gradients (Fig. 9) lie outside the locus of quiescent ETGs with $(u-r)$ gradients a factor of ~2 steeper than those seen in the quiescent ETGs. Such steepened colour gradients (i.e. redder core colours) have been previously identified in nearby, luminous elliptical galaxies with optical dust features (Kim & Im 2013) and are likely seeded from accretion of a gas-rich satellite (Martini, Dicken & Storchi-Bergmann 2013). Additionally, these galaxies possess circumnuclear blue rings (Fig. 2) associated with rejuvenation of quiescent stellar systems (Shapiro et al. 2010), consistent with a frosting interpretation.

Both the global and core colours of the dust-ring pE galaxy (nyu674881) reside in the gap between star-forming and quiescent galaxies. Its relatively flat colour gradient is consistent with local quiescent ETGs; the dust ring appears to have little effect on the its colour gradient in contrast to the other two galaxies in this region. Yet, previous analysis of elliptical galaxies with prominent optical dust lanes (rings) indicates that these features represent a transition phase between starburst and quiescence and implicate recent gas-rich minor (i.e. $M_{1,*}: M_{2,*} \gtrsim 4$) merging as their likely cause (Shabala et al. 2012). The capture of a gas-rich satellite via minor merging has been shown to induce low-level star formation consistent with a frosting interpretation (Kaviraj et al. 2009). We note that if minor merging is responsible for the enhanced star formation, the galaxy's generally smooth morphology indicates that the star formation lifetime appears to be greater than the time for the interaction features to disappear. Overall, all three galaxies from region 2 of the Balmer–$D_n(4000)$ plane lack the clearly young spectral signatures and blue core colours seen in the more disturbed SPM and pE/SPM galaxies and are hence not as likely to be remnants of recent major mergers.

4.3 Many paths into the green valley?

The five galaxies that principally lie in the third region of the Balmer–$D_n(4000)$ plane exhibit a tight clustering of both radial indices with a generally negative (i.e. smaller values at larger radii) slope in their 4000-Å break strengths and a positive slope in their Balmer absorption values (Fig. 7). The central $D_n(4000)$ index

values in these galaxies are the largest seen at any radius of any galaxy in our sample suggesting that these galaxies are the least likely to be remnants of *recent* gas-rich major mergers due to old ($\gtrsim 5$ Gyr) populations in their cores. The overall decreasing 4000-Å break strength and increasing (but still negative) Balmer absorption at large radii are consistent with population gradients seen in the general population of nearby ETGs (Sánchez-Blázquez et al. 2006; González Delgado et al. 2014). The anomalous large, positive Balmer absorption value seen at the sixth annulus of nyu619567 is likely a measurement error stemming from an overfitting of the H δ_A absorption feature (see Fig. C1).

These galaxies have quiescent global and core colours with small, negative gradients (i.e. slightly redder core colours, Fig. 9) consistent with the locus of local quiescent ETGs. Their stellar masses[8] are in excess of 3×10^{10} M$_\odot$ – the characteristic mass above which local galaxies tend to have little star formation and increasingly become bulge-dominated ellipticals (Kauffmann et al. 2003b). These galaxies have a median scatter in their ($g-r$) colours bluewards from the empirical red/blue dividing line in Fig. 1 of ~0.03 mag. This is within the typical colour error (0.04 mag) found by M14 and may account for their apparent green-valley colours. It is also possible that these galaxies, like those found in region 2, may be red sequence galaxies which have migrated into the green valley. Notably, however, they lack the Balmer absorption seen in the region 2 galaxies and have luminosity-weighted ages at least 1–2 Gyr older.

The galaxies in region 3 present a rather homogeneous group reminiscent of local relaxed ellipticals with smooth cores, quiescent colours, steep index gradients, and no dust features. Further, all of the elliptical (i.e. not SPM) galaxies in our sample classified as pE owing to outer asymmetries (e.g. nyu916578) lie in this region. This is surprising as we argued previously that the galaxies in region 2 are likely to be remnants of minor mergers, but those galaxies lack the structural signatures of recent interaction (i.e. arms, loops, shells, etc.) seen in these pE galaxies. This raises the important question as to how the galaxies in region 3 could plausibly come about.

It is well known that mergers between equal-mass disc galaxies result in remnants with tidal tails and plumes (Toomre & Toomre 1972; Barnes 1988, 1992), but the low surface brightness of these and other late-stage features (e.g. small loops, arms, and shells) are also seen in minor mergers (Feldmann, Mayer & Carollo 2008) making discriminating between these two types of merger remnants difficult (Lotz et al. 2008; Struck & Smith 2012). Further, not all morphologically disturbed ellipticals are star forming (Michard & Prugniel 2004), and not all blue (presumably star-forming) ellipticals are morphologically disturbed (see nyu22318 in our sample). Yet both plausible formation histories predict the low-level star formation observed in nearby ETGs (e.g. Yi et al. 2005). Additionally, a scenario in which an existing elliptical galaxy undergoes a (nearly) equal-mass gas-rich merger would leave behind a remnant with such late-stage features. These so-called 'mixed' mergers have been shown to be important in explaining the dichotomy of local elliptical galaxies (Rothberg & Joseph 2006b). However, their general importance in galaxy evolution is not well constrained (Khochfar & Burkert 2003).

The modestly disturbed morphologies and quiescent colours of the galaxies in region 3 may be described by yet another merger scenario: dissipationless (so-called dry) major mergers. In this scenario, two gas-poor elliptical galaxies merge, producing a remnant with broad, low surface brightness features (Bell et al. 2006) like

[8] Using $h = 0.7$.

those seen in many of the pE galaxies in our sample. Assuming the progenitor galaxies possess colours slightly redder than our empirical red/blue dividing line, such a dry merger would conserve colour but allow the remnant to cross our dividing line; producing a slightly bluer-than-usual elliptical galaxy at a given stellar mass (Skelton, Bell & Somerville 2009). However, simulations from Kawata et al. (2006) show that the colour and structure of such features can also be produced through spheroid-disc gas-rich *minor* mergers. The same complications listed above for mixed-mergers then apply to this scenario, as well. Sánchez-Blázquez et al. (2009) found that half of the ellipticals from van Dokkum (2005) having strong tidal features exhibit a 'frosting' of star formation like that seen in our sample of galaxies in region 2. These frosted ellipticals were also found to be supported by rotation, indicating the presence of a dynamically cold stellar component. This is in contrast to simulations of dry mergers which produce remnants with dispersion-dominated kinematics similar to those of local cluster galaxies (Naab et al. 2006; Naab & Ostriker 2009). While our sample of galaxies in region 3 is inconsistent with the frosting scenario, it follows that a careful analysis of the kinematic structure of these galaxies could be used to plausibly identify if dry mergers may play a role in their assembly.

It is clear, then, that there are many routes a galaxy may take to arrive in region 3 of the Balmer–$D_n(4000)$ plane. Extracting the precise SFH for these galaxies requires analysis outside the scope of this work. However, we note that in Fig. 7, the galaxy nyu916578 stands out among the others in region 3 in that its three outermost radial indices track into the fourth region of the Balmer–$D_n(4000)$ plane near the burst models with luminosity-weighted ages of ~1 Gyr and exhibit Balmer absorption consistent with an increased fraction of young stars. This is highly contrasted by its core population with ages closer to ~10 Gyr. Such population gradients have been seen in 'revitalized' elliptical galaxies consistent with ongoing star formation in their outer annuli associated with tidal stripping during a gas-rich *minor* merger (Fang et al. 2012). The presence of younger stellar populations at large galactic radii is consistent with the outside-in formation scenario of elliptical galaxies and offers a possible explanation for observed 'inverted' age gradients and lower metallicity at large radii in some local elliptical galaxies (e.g. Baes et al. 2007; La Barbera et al. 2010).

5 DISCUSSION

Using the predictions of the modern merger hypothesis as a guide, we measure the radial Balmer and $D_n(4000)$ indices to attempt to distinguish between galaxies originating from a recent, gas-rich major merger and those undergoing some other mass assembly mechanism. In Section 4, we present a detailed analysis combining the radial indices, optical colours, and morphological features to examine the SFHs of our sample of galaxies. With those details in mind, we show a characteristic 'decision' tree (Fig. 11) for our sample which allows us to a posteriori correlate the characteristics of each galaxy in our sample with its location in the qualitatively defined regions of the Balmer–$D_n(4000)$ plane.

We begin by splitting our sample into two groups using the presence of strong outer loops. This cleanly separates strongly disturbed SPM signatures (i.e. $T_{ppm} \geq 10$) from ellipticals with smooth or modestly disturbed morphologies. For the most disturbed galaxies, we further examine whether they are consistent with undergoing a strong central burst of star formation. As discussed in Section 4.1, the key distinction between galaxies residing in regions 1 and 4 appears to be only the strength of the burst and not the *existence*
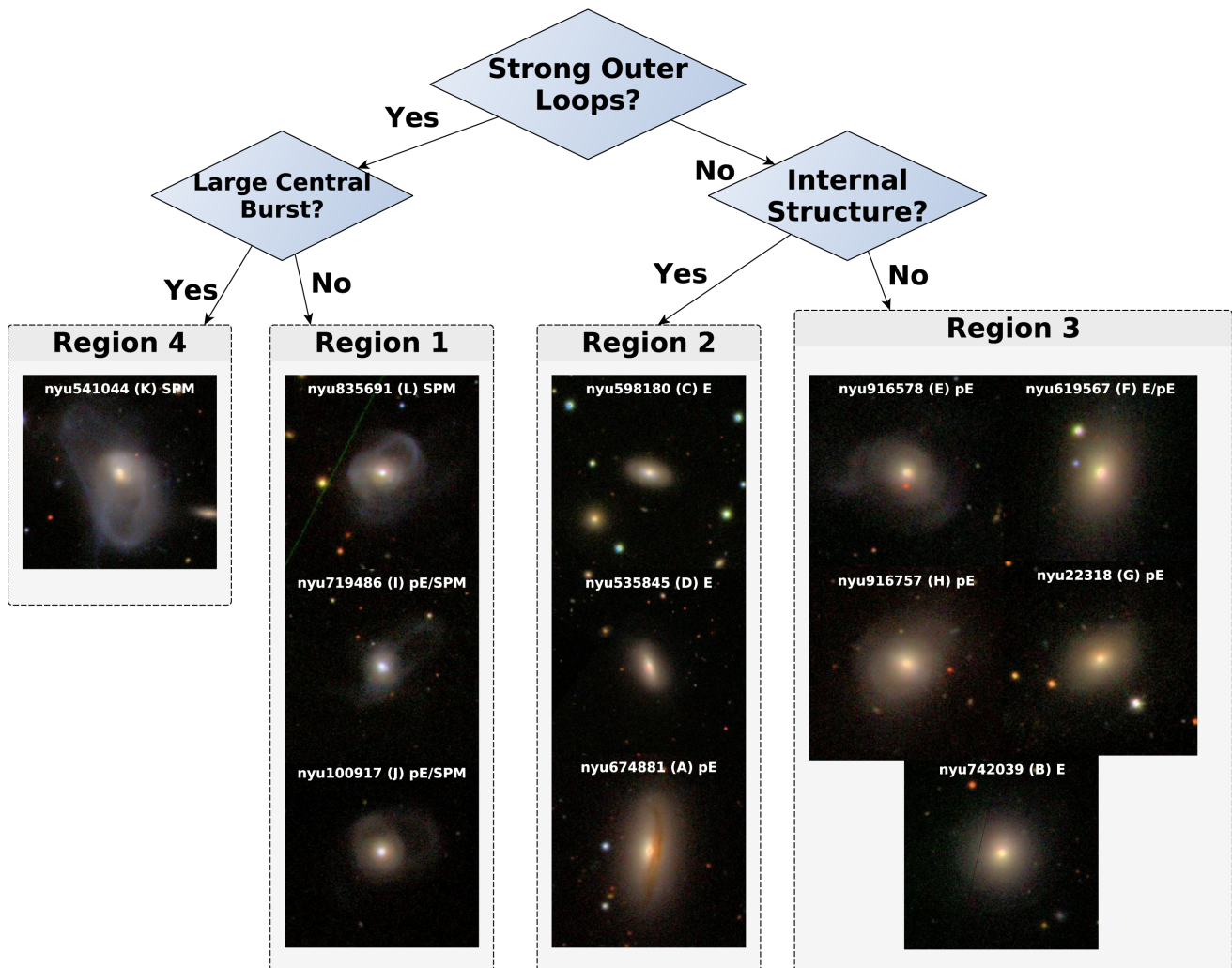
Figure 11. A characteristic 'decision' tree for the classification of our sample of massive, blue spheroidal galaxies. The images come from the SDSS and are scaled to $40\,\mathrm{kpc}h^{-1}$ on a side. At the top of each image, we list the name, single-letter designation, and morphological classification from Table 1. The T_{ppm} and morphological characteristics are detailed in Section 2.1. Each large box represents one of the regions of the Balmer–$D_n(4000)$ plane as described in Section 3.1. A color version is available in the online journal.

of a burst. Further, we find that galaxies in region 4 appear to be consistent with E+A or post-starburst galaxies. However, we note that our small sample statistics preclude extending this result further. Galaxies in region 1 of the index plane are consistent with a dichotomy of SFHs from long-lived, continuous star formation to a recent, weak burst, forming ≤5 per cent of their mass in a recent burst.

For the second half of the tree, we find that galaxies with smooth elliptical morphologies but internal structures such as circumnuclear blue rings or dust lanes preferentially reside in region 2 of the index plane. Additionally, they possess flat gradients in their 4000-Å break strengths, but have radial Balmer absorption indices consistent with a changing fraction of young stars atop a uniform, older population. As outlined in Section 4.2, previous examination of galaxies with similar internal structures attribute these features to revitalized stellar populations brought on by minor merger events – in agreement with our frosting interpretation. This is in accord with the general idea that minor mergers are thought to play a significant role in evolving spheroidal galaxies for two reasons: (i) the small number of major mergers in the local Universe cannot provide the abundance of green-valley ETGs (Darg et al. 2010; Salim & Rich

2010; Lotz et al. 2011), and (ii) the observed size evolution of elliptical galaxies since $z \sim 1$ is best explained by growth dominated by minor mergers (Bezanson et al. 2009; Naab, Johansson & Ostriker 2009; Oser et al. 2012; Bédorf & Portegies Zwart 2013; Hilz, Naab & Ostriker 2013; Lee et al. 2013).

Moving to the final branch of the decision tree, we anticipate finding smooth (i.e. small T_{ppm} values) galaxies with SFHs least like those predicted in the modern merger hypothesis. Indeed, all but one of the galaxies in region 3 have SFHs much like local quiescent ETGs. However, many of them exhibit external structures such as arms or loops, and all of the elliptical (i.e. *not* SPM) galaxies labelled as pE owing to these outer asymmetries (e.g. nyu916578) lie in this region. The one galaxy which runs counter to this general interpretation is nyu916578 which exhibits a strong, negative age gradient with stellar populations at its largest radii having luminosity-weighted ages ≲1 Gyr. Such 'inverted' age gradients are attributable to gas-rich minor merging. Overall, the galaxies in region 3 have a scatter in their $(g-r)$ colours of only $\sim$0.03 mag bluewards of the empirical red/blue dividing line (Fig. 1) and lack clear indications of ongoing star formation. It is likely that their green-valley colours will quickly fade and migrate them on to the red sequence.

Additionally, they possess stellar masses near $\sim 10^{10.8}$ M$_\odot$ h^{-2} and extinction- and k-corrected SDSS absolute r-band magnitudes between $-21 \le M_r \le -22$ (Table 1), placing them close to the knee of the green-valley luminosity function found by Gonçalves et al. (2012), consistent with the downsizing of the red sequence (i.e. the low-mass end of the red sequence is populated at late times).

Previous detailed examination of green valley galaxies revealed a dichotomy in their morphologies (Schawinski et al. 2014). The presence of both early- and late-type galaxies in the green valley lends support to the idea that multiple mass-assembly mechanisms are likely responsible for galaxy growth over cosmic time. Our targeted study of spheroidal galaxies with blue sequence colours expands on that work, demonstrating a further branching of mass assembly histories even within just ETGs in the green valley. This indicates that the green valley is a rich laboratory for studying the transitory phases of galaxy formation and evolution. Our analysis could only be accomplished via the usage of spatially resolved spectroscopy and motivates the study of green valley galaxies in large IFU surveys.

6 SUMMARY AND CONCLUSIONS

In this work, we have combined visual morphologies with spatially resolved spectra and optical colours to characterize the radial SFHs of a unique sample of plausible new ellipticals. Utilizing techniques for examining SFHs previously used to characterize the central regions of local galaxies (e.g. K03), we compare the stellar age indices H δ, H γ, and the 4000 Å break to synthetic SFH models at radii from the core out to $\sim$2–3 half-light radii. We find that these index values and their radial dependence correlate with specific morphological features such that the most disturbed galaxies have the smallest 4000-Å break strengths and the largest Balmer absorption values. With this new spatial data, we are able to detect the presence of a centrally concentrated starburst occurring within the last $\sim$1 Gyr – allowing us to plausibly discriminate between the construction of *new* ellipticals by gas-rich major merging following the modern merger hypothesis (Hopkins et al. 2008b) and ellipticals undergoing other mass assembly mechanisms.

Our main conclusions are as follows.

(i) We find that one-third of our sample possess the strong morphological disturbances and central star formation consistent with being plausible remnants of a recent, gas-rich major merger. However, only one of them exhibits the characteristics of having recently undergone a strong, centrally concentrated burst of star formation followed by quenching. Its quiescent optical colours and strong burst signature are consistent with its well-known status as an E+A (post-starburst) galaxy. Assuming our small sample comports with the population of local merger remnants, we infer that the modern merger hypothesis describes the assembly of only $\sim$25 per cent of plausible major merger remnants in the local Universe.

(ii) Three of the four plausible major mergers in our sample have star-forming optical colours with much bluer centres. Their Balmer absorption and 4000-Å break strength index values indicative of having centrally concentrated young stellar populations. However, they lack the clear signatures of a recent, *strong* central burst of star formation. Overall, their SFHs are generally consistent with having formed $\sim$5 per cent of their stellar mass in a recent, weak burst.

(iii) Two-thirds of our sample of 12 massive ($M_* \ge 10^{10}$ M$_\odot$), nearby ($z \le 0.03$), visually selected plausible new ellipticals with blue-sequence optical colours and varying degrees of morphological peculiarities are inconsistent with the predictions from simulations of gas-rich major mergers. We therefore find that their mass assembly histories are not well-described by the modern merger hypothesis. Half of these galaxies exhibit characteristics seen in remnants of recent, gas-rich *minor* mergers and the other half have radial SFHs consistent with those seen in local quiescent ellipticals.

REFERENCES

Adelman-McCarthy J. K. et al., 2006, ApJS 162, 38
Bacon R. et al., 2001, MNRAS, 326, 23
Baes M., Sil'chenko O. K., Moiseev A. V., Manakova E. A., 2007, A&A, 467, 991
Baldry I. K., Glazebrook K., Brinkmann J., Ivezić v., Lupton R. H., Nichol R. C., Szalay A. S., 2004, ApJ, 600, 681
Balogh M. L., Morris S. L., Yee H. K. C., Carlberg R. G., Ellingson E., 1999, ApJ, 527, 54
Barnes J. E., 1988, ApJ, 331, 699
Barnes J. E., 1992, ApJ, 393, 484
Barnes J. E., Hernquist L. E., 1991, ApJ, 370, L65
Barnes J. E., Hernquist L., 1996, ApJ, 471, 115
Bédorf J., Portegies Zwart S., 2013, MNRAS, 431, 767
Bell E. F., McIntosh D. H., Katz N., Weinberg M. D., 2003, ApJS, 149, 289
Bell E. F. et al., 2004a, ApJ, 600, L11
Bell E. F. et al., 2004b, ApJ, 608, 752
Bell E. F. et al., 2006, ApJ, 640, 241
Bell E. F., Zheng X. Z., Papovich C., Borch A., Wolf C., Meisenheimer K., 2007, ApJ, 663, 834
Bell E. F. et al., 2012, ApJ, 753, 167
Bershady M. A., Andersen D. R., Harker J., Ramsey L. W., Verheijen M. A. W., 2004, PASP, 116, 565
Bezanson R., van Dokkum P. G., Tal T., Marchesini D., Kriek M., Franx M., Coppi P., 2009, ApJ, 697, 1290

Blanton M. R., 2006, ApJ, 648, 268
Blanton M. R. et al., 2005, AJ, 129, 2562
Brammer G. B. et al., 2009, ApJ, 706, L173
Brown M. J. I., Dey A., Jannuzi B. T., Brand K., Benson A. J., Brodwin M., Croton D. J., Eisenhardt P. R., 2007, ApJ, 654, 858
Bruzual G., Charlot S., 2003, MNRAS, 344, 1000
Cappellari M., Copin Y., 2003, MNRAS, 342, 345
Cappellari M. et al., 2011, MNRAS, 413, 813
Charlot S., Fall S. M., 2000, ApJ, 539, 718
Cid Fernandes R. et al., 2013, A&A, 557, A86
Cortese L., Hughes T. M., 2009, MNRAS, 400, 1225
Cox T. J., Jonsson P., Primack J. R., Somerville R. S., 2006, MNRAS, 373, 1013
Cox T. J., Jonsson P., Somerville R. S., Primack J. R., Dekel A., 2008, MNRAS, 384, 386
Darg D. W. et al., 2010, MNRAS, 401, 1043
Dressler A., Gunn J. E., 1983, ApJ, 270, 7
Eliche-Moral M. C. et al., 2010, A&A, 519, 55
Faber S. M. et al., 2007, ApJ, 665, 265
Falco E. E. et al., 1999, PASP, 111, 438
Fang J. J., Faber S. M., Salim S., Graves G. J., Rich R. M., 2012, ApJ, 761, 23
Feldmann R., Mayer L., Carollo C. M., 2008, ApJ, 684, 1062
Fukugita M., Nakamura O., Turner E. L., Helmboldt J., Nichol R. C., 2004, ApJ, 601, L127
Gallazzi A., Charlot S., Brinchmann J., White S. D. M., Tremonti C. A., 2005, MNRAS, 362, 41
Gonçalves T. S., Martin D. C., Menéndez-Delmestre K., Wyder T. K., Koekemoer A., 2012, ApJ, 759, 67
González Delgado R. M. et al., 2014, A&A, 562, A47
Goto T., 2004, A&A, 427, 125
Goto T., Kawai A., Shimono A., Sugai H., Yagi M., Hattori T., 2008, MNRAS, 386, 1355
Hibbard J. E., Yun M. S., 1999, ApJ, 522, L93
Hilz M., Naab T., Ostriker J. P., 2013, MNRAS, 429, 2924
Holden B. P., van der Wel A., Rix H.-W., Franx M., 2012, ApJ, 749, 96
Hopkins P. F., Hernquist L., Cox T. J., Robertson B., Springel V., 2006, ApJS, 163, 50
Hopkins P. F., Hernquist L., Cox T. J., Kereš D., 2008a, ApJS, 175, 356
Hopkins P. F., Cox T. J., Kereš D., Hernquist L., 2008b, ApJS, 175, 390
Husemann B. et al., 2013, A&A, 549, 87
Kauffmann G., White S. D. M., Guiderdoni B., 1993, MNRAS, 264, 201
Kauffmann G. et al., 2003a, MNRAS, 341, 33 (K03)
Kauffmann G. et al., 2003b, MNRAS, 341, 54
Kaviraj S., Peirani S., Khochfar S., Silk J., Kay S., 2009, MNRAS, 394, 1713
Kawata D., Mulchaey J. S., Gibson B. K., Sánchez-Blázquez P., 2006, ApJ, 648, 969
Kelz A. et al., 2006, PASP, 118, 129
Khochfar S., Burkert A., 2003, ApJ, 597, L117
Khochfar S., Silk J., 2006, ApJ, 648, L21
Kim D., Im M., 2013, ApJ, 766, 109
Kormendy J., 2009, in Jogee S., Marinova I., Hao L., Blanc G. A., eds, ASP Conf. Ser. Vol. 419, Galaxy Evolution: Emerging Insights and Future Challenges. Astron. Soc. Pac., San Francisco, p. 87
La Barbera F., De Carvalho R. R., De La Rosa I. G., Gal R. R., Swindle R., Lopes P. A. A., 2010, AJ, 140, 1528
Lee J. H., Lee M. G., Hwang H. S., 2006, ApJ, 650, 148
Lee J. H. et al., 2013, ApJ, 762, L4
Lotz J. M., Jonsson P., Cox T. J., Primack J. R., 2008, MNRAS, 391, 1137
Lotz J. M., Jonsson P., Cox T. J., Croton D., Primack J. R., Somerville R. S., Stewart K., 2011, ApJ, 742, 103
McIntosh D. H. et al., 2014, MNRAS, 442, 533 (M14)
Martin D. C. et al., 2007, ApJS, 173, 342
Martini P., Dicken D., Storchi-Bergmann T., 2013, ApJ, 766, 121
Mast D. et al., 2014, A&A, 561, A129
Michard R., Prugniel P., 2004, A&A, 423, 833

Mihos J. C., Hernquist L., 1996, ApJ, 464, 641
Moustakas J. et al., 2013, ApJ, 767, 50
Naab T., Ostriker J. P., 2009, ApJ, 690, 1452
Naab T., Khochfar S., Burkert A., 2006, ApJ, 636, L81
Naab T., Johansson P. H., Ostriker J. P., 2009, ApJ, 699, L178
Norton S. A., Gebhardt K., Zabludoff A. I., Zaritsky D., 2001, ApJ, 557, 150
Oser L., Naab T., Ostriker J. P., Johansson P. H., 2012, ApJ, 744, 63
Papaderos P. et al., 2013, A&A, 555, L1
Pracy M. B., Owers M. S., Couch W. J., Kuntschner H., Bekki K., Briggs F., Lah P., Zwaan M., 2012, MNRAS, 420, 2232
Rosales-Ortega F. F., Kennicutt R. C., Sánchez S. F., Díaz A. I., Pasquali A., Johnson B. D., Hao C. N., 2010, MNRAS, 405, 735
Roth M. M. et al., 2005, PASP, 117, 620
Rothberg B., Joseph R. D., 2006a, AJ, 131, 185
Rothberg B., Joseph R. D., 2006b, AJ, 132, 976
Salim S., Rich R. M., 2010, ApJ, 714, L290
Sánchez S. F., 2006, Astron. Nachr., 327, 850
Sánchez S. F. et al., 2004, ApJ, 614, 586
Sánchez S. F., Rosales-Ortega F. F., Kennicutt R. C., Johnson B. D., Diaz A. I., Pasquali A., Hao C. N., 2011, MNRAS, 410, 313
Sánchez S. F. et al., 2012, A&A, 538, 8
Sánchez-Blázquez P., Gorgas J., Cardiel N., 2006, A&A, 457, 823
Sánchez-Blázquez P., Gibson B. K., Kawata D., Cardiel N., Balcells M., 2009, MNRAS, 400, 1264
Schawinski K., Thomas D., Sarzi M., Maraston C., Kaviraj S., Joo S.-J., Yi S. K., Silk J., 2007, MNRAS, 382, 1415
Schawinski K. et al., 2009, MNRAS, 396, 818
Schawinski K., Dowlin N., Thomas D., Urry C. M., Edmondson E., 2010, ApJ, 714, L108
Schawinski K. et al., 2014, MNRAS, 440, 889
Schlegel D. J., Finkbeiner D. P., Davis M., 1998, ApJ, 500, 525
Schweizer F., 1996, AJ, 111, 109
Serra P., Trager S. C., 2007, MNRAS, 374, 769
Shabala S. S. et al., 2012, MNRAS, 423, 59
Shapiro K. L. et al., 2010, MNRAS, 402, 2140
Skelton R. E., Bell E. F., Somerville R. S., 2009, ApJ, 699, L9
Snyder G. F., Cox T. J., Hayward C. C., Hernquist L., Jonsson P., 2011, ApJ, 741, 77
Springel V., Di Matteo T., Hernquist L., 2005, ApJ, 620, L79
Stoughton C. et al., 2002, AJ, 123, 485
Strateva I. et al., 2001, AJ, 122, 1861
Struck C., Smith B. J., 2012, MNRAS, 422, 2444
Sturch L. K., Madore B. F., 2012, in Tuffs R. J., Popescu C. C., eds, Proc. IAU Symp. 284, The Spectral Energy Distribution of Galaxies. Cambridge Univ. Press, Cambridge, p. 180
Thilker D. A. et al., 2010, ApJ, 714, L171
Tojeiro R. et al., 2013, MNRAS, 432, 359
Toomre A., Toomre J., 1972, ApJ, 178, 623
Trager S. C., Faber S. M., Worthey G., González J. J., 2000a, AJ, 119, 1645
Trager S. C., Faber S. M., Worthey G., González J. J., 2000b, AJ, 120, 165
Trujillo I. et al., 2006, ApJ, 650, 18
Trujillo I., Conselice C. J., Bundy K., Cooper M. C., Eisenhardt P., Ellis R. S., 2007, MNRAS, 382, 109
van Dokkum P. G., 2001, PASP, 113, 1420
van Dokkum P. G., 2005, AJ, 130, 2647
Vazdekis A., Sánchez-Blázquez P., Falcón-Barroso J., Cenarro A. J., Beasley M. A., Cardiel N., Gorgas J., Peletier R. F., 2010, MNRAS, 404, 1639
Weijmans A. et al., 2009, MNRAS, 398, 561
White S. D. M., Rees M. J., 1978, MNRAS, 183, 341
Wild V., Walcher C. J., Johansson P. H., Tresse L., Charlot S., Pollo A., Le Fèvre O., de Ravel L., 2009, MNRAS, 395, 144
Worthey G., Ottaviani D. L., 1997, ApJS, 111, 377
Yang X., Mo H. J., van den Bosch F. C., Pasquali A., Li C., Barden M., 2007, ApJ, 671, 153
Yi S. K. et al., 2005, ApJ, 619, L111
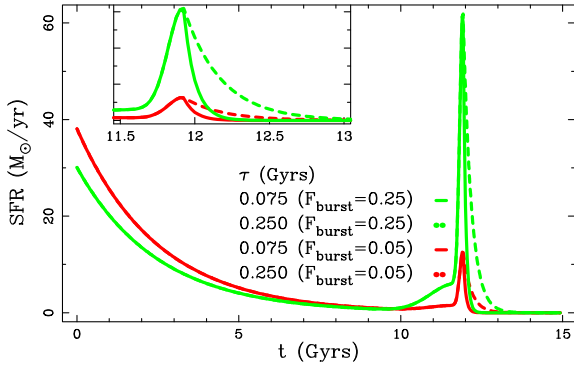York D. G. et al., 2000, AJ, 120, 1579

Figure A1. SFRs as a function of time (i.e. the SFHs) for four of our constructed burst models used throughout the rest of this work: in two in which 25 per cent of the total galaxy mass is formed in a single burst (green) and two burst models with a 5 per cent burst fraction (red). The solid lines refer to short e-folding times of 75 Myr and the dashed lines to long e-folding times of 250 Myr. The bursts are triggered at redshift 0.12 when the galaxy is ~12 Gyr old. Inset: zoom-in of SFHs near the burst. A color version is available in the online journal.

APPENDIX A: CONSTRUCTING BURST MODELS

A key prediction of the modern merger hypothesis is that merging galaxies with favourable gas dynamics undergo a centrally concentrated burst of star formation. To determine if the SFHs of our observed galaxies are consistent with this scenario, we construct a suite of synthetic SEDs that model the abrupt change in star formation during the merger process. We begin with a continuous SFH model assuming an exponentially decreasing star-formation rate, $\mathrm{SFR_{bg}}(t) = \alpha_0 e^{-t/\tau_0}$, where α_0 is the SFR at $t = 0$ and τ_0 is the characteristic time. Atop this background of continuous star formation, we add Gaussians of fixed widths and amplitudes to model the bursts during the merger process. To make our models as realistic as possible, we use two bursts: a small-amplitude, large width (i.e. long-lasting) burst representing star formation induced by tidal interaction, and a second burst with large-amplitude and small width representing the starburst induced by coalescence (see Fig. A1). The modern merger hypothesis also predicts the ignition of an AGN that provides a source of energetic feedback to quench star formation in the galaxy. To model this AGN, we impose an exponentially decreasing SFR once the second burst has reached its peak to quench the star formation.

Using t_i for the time of tidal interaction and t_c for the time of coalescence, the SFR due to both bursts is given by

$$\mathrm{SFR_b}(t) = [G_i + G_c]\, g(t)$$

with

$$G_x(t) = \alpha_x \exp\left\{-(t - t_x)^2/2\sigma_x^2\right\}$$

and

$$g(t) = \begin{cases} 1 & t < t_c \\ \exp\{-t/\tau_b\} & t \geq t_c, \end{cases}$$

where t_x is one of t_i or t_c, α_x is the burst amplitude at $t = t_x$, σ_x is the width of the respective burst, and τ_b is the characteristic time for the exponentially declining SFR of the burst at coalescence. The fraction of stars formed (by mass) during the burst, F_{burst}, is defined as

$$F_{\mathrm{burst}} = \frac{\text{stellar mass formed during burst}}{\text{total stellar mass}}.$$

Incorporating our definitions from above, this becomes

$$
\begin{aligned}
F_{\mathrm{burst}} &= \frac{\int_{t_0}^{t_f} \mathrm{SFR_b}(t)\, dt}{\int_{t_0}^{t_f} \mathrm{SFR_{bg}}(t) + \mathrm{SFR_b}(t)\, dt} \\
&= \frac{\int_{t_0}^{t_f} [G_i + G_c]\, g(t)\, dt}{\int_{t_0}^{t_f} \left[\alpha_0 \exp\{-t/\tau_0\} + G_i + G_c\right] g(t)\, dt},
\end{aligned}
\tag{A1}
$$

where $\mathrm{SFR_{bg}}$ is the SFR of the background model. We assume that this background star formation continues during the burst such that the total number of stars formed is the background star formation plus the two bursts.

Clearly, there are many parameters to be tuned in this formula. We choose to keep constant the widths of the bursts and the characteristic time of the background star formation. Specifically, we assume a total galaxy lifetime $t_f = t_c + 3$ Gyr, a characteristic time of $\tau_0 = 2.5$ Gyr for the background star formation, an interaction time of $t_i = t_c - 250$ Myr, an interaction burst width of $\sigma_i = 750$ Myr, and a coalescence burst width of $\sigma_c = 100$ Myr. These parameters are consistent with the results of gas-rich major merger simulations from Cox et al. (2008). Finally, we normalize the total (background plus bursts) star formation such that a mass of $\mathrm{M_{tot}}$ is formed.

The amplitudes of the Gaussian bursts are independent of time, so we can rearrange the integrals in equation (A1) using the substitutions

$$\gamma_1 = \int_{t_0}^{t_f} \exp\left\{-(t - t_i)^2/2\sigma_i^2\right\} g(t)\, dt$$

$$\gamma_2 = \int_{t_0}^{t_f} \exp\left\{-(t - t_c)^2/2\sigma_c^2\right\} g(t)\, dt$$

$$\gamma_3 = \int_{t_0}^{t_f} \exp\{-t/\tau_0\}\, g(t)\, dt$$

to generate a set of simple algebraic expressions to constrain the peak SFR parameters α_0, α_c, and α_i such that

$$\alpha_i \gamma_1 + \alpha_c \gamma_2 = \mathrm{M_{tot}} - \alpha_0 \gamma_3$$

$$\alpha_i \gamma_1 + \alpha_c \gamma_2 = \frac{F_{\mathrm{burst}}}{1 - F_{\mathrm{burst}}} \alpha_0 \gamma_3.$$

If we assume the peak SFR of the interaction and coalescence bursts are tied such that $\alpha_i = k\alpha_c$, then we arrive at our final expressions for the peak SFR parameters

$$\alpha_0 = \frac{\mathrm{M_{tot}}(1 - F_{\mathrm{burst}})}{\gamma_3}$$

$$\alpha_c = \frac{\mathrm{M_{tot}} F_{\mathrm{burst}}}{(k\gamma_1 + \gamma_2)}.$$

Using this model, we parametrize the SFH of our burst models using four parameters: the burst fraction F_{burst}, the relative strength of the peak SFR of the two bursts k, the characteristic time of the post-coalescence exponentially decaying SFR τ_b, and the total mass formed. We assume $k = 0.1$ and $\mathrm{M_{tot}} = 10^{11}\,\mathrm{M_\odot}$ throughout, but generate our suite of burst models based on a variety of burst fractions and characteristic times. See Section 3 for these values.

APPENDIX B: INDEX MODEL PLANE

In Fig. B1, we present the detailed Balmer–$D_n(4000)$ index plane for each galaxy in our sample. For each galaxy, we show the suite of models outlined in Section 3. The inset in each figure shows the
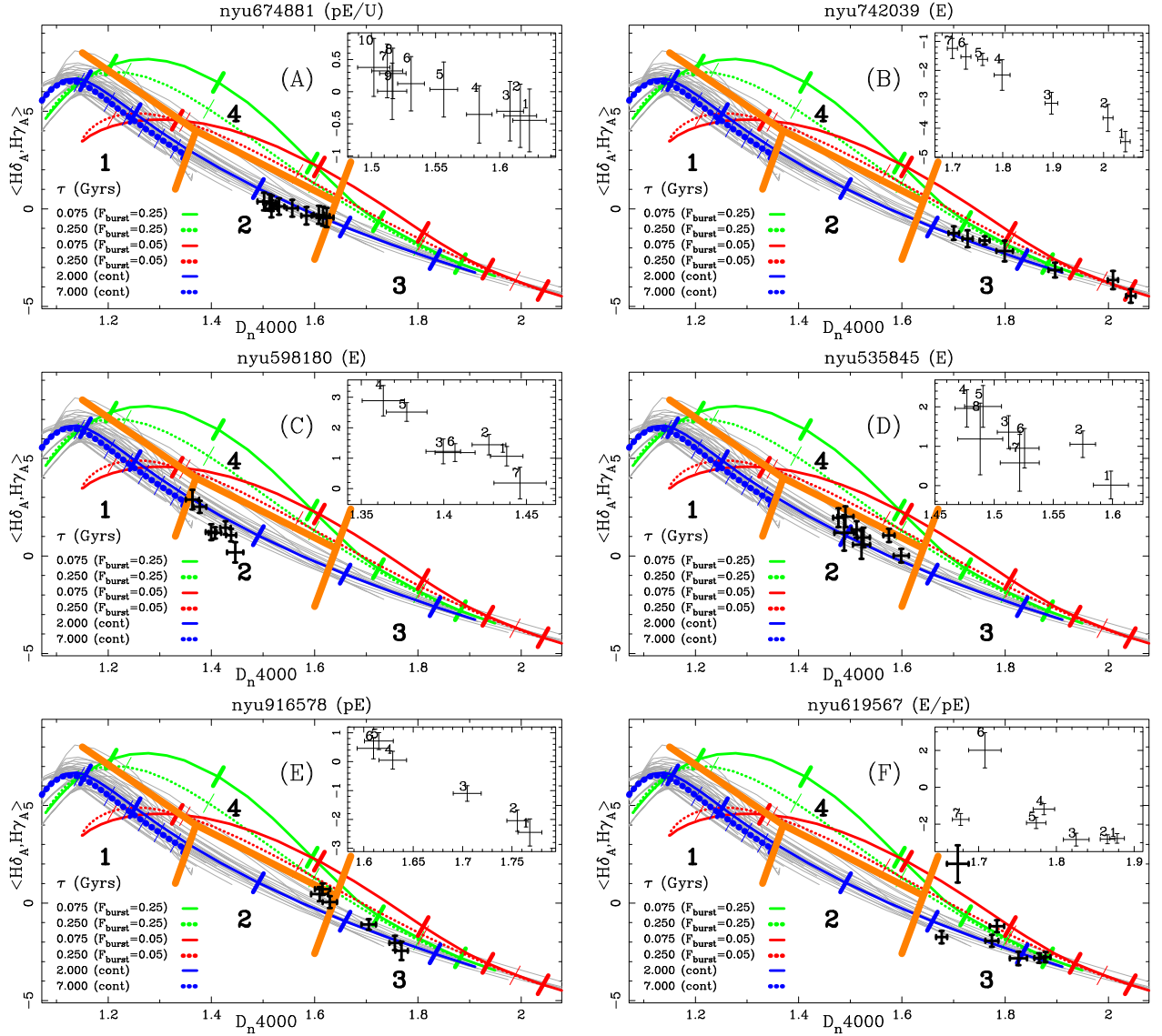
Figure B1. The stellar Balmer absorption versus 4000-Å break strength model plane showing two continuous SFH models (blue) and two burst models (green) covering a range of e-folding times permitted for each model type. The full suite of continuous SFH models are shown in light grey. Tick marks denote points along the model lines with known ages. For the continuous models, the ages are 1, 3, 5, 7, 9, and 11 Gyr. For the burst models, the ages are 0.2, 0.5, 0.9, 1.5, and 2.5 Gyr. The four qualitative regions from the text are labelled and the large orange lines mark their approximate boundaries. At the top of each panel, we give the galaxy's morphological classification next to its name. Inset: zoom-in to the plane showing the indices marked in annulus order. A color version is available in the online journal.

radial order of the index measurements with 1 indicating the central annulus.

APPENDIX C: RADIAL SPECTRA

In Fig. C1, we present the radially binned, emission-subtracted spectra for each galaxy in our sample. The number of spec-

tra is determined by an S/N cut-off outlined in Section 2.3.2. The spectra are listed top-to-bottom from the centre to the outermost annulus. For the central spectrum, we label several well-known spectral lines. Note, that due to the spectra being produced on different spectrographs with varying setups (see Section 2.2 for details), the wavelength coverage is not the same for each galaxy.
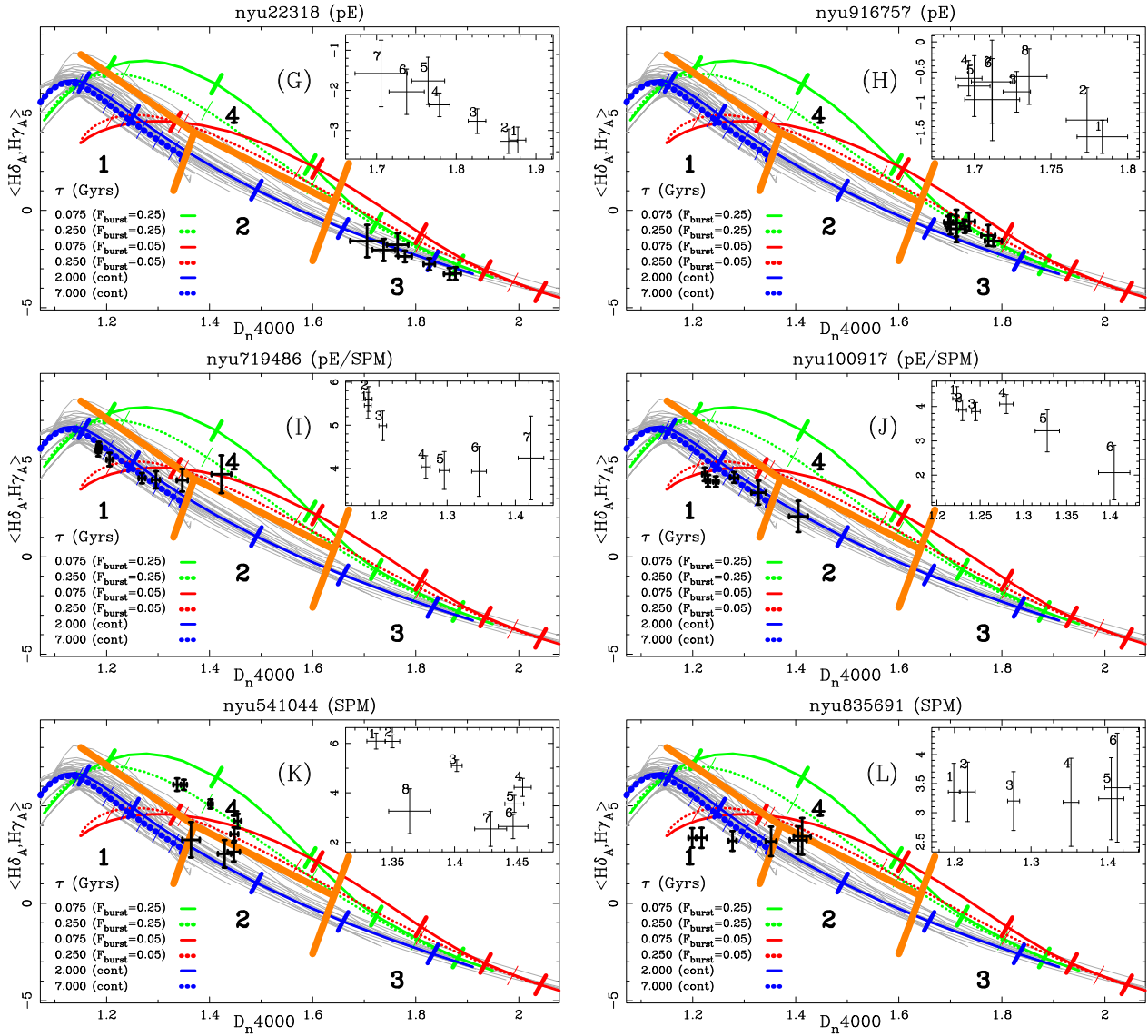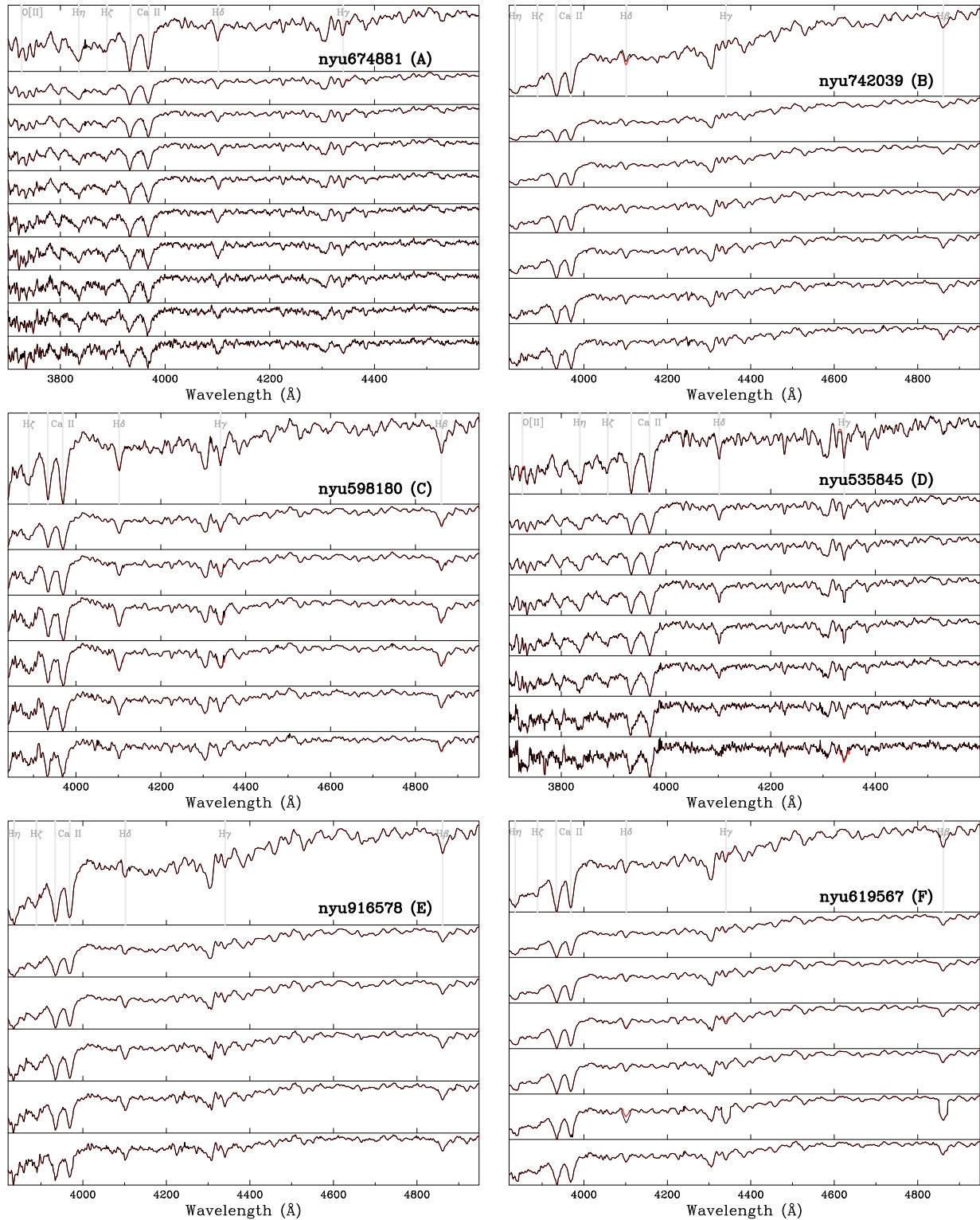
Figure B1 – *continued*

Figure C1. Observed spectrum (red) and emission-subtracted spectrum (grey) for each annulus with S/N pixel^{-1} >10 from each galaxy in our sample. Each spectrum is scaled to arbitrary flux units to show detail and given in annulus order from top to bottom with the central annulus at the top. For the central annulus, several well-known spectral features such as the hydrogen Balmer series and the Ca II lines are highlighted with grey vertical lines and labelled accordingly. A color version is available in the online journal.
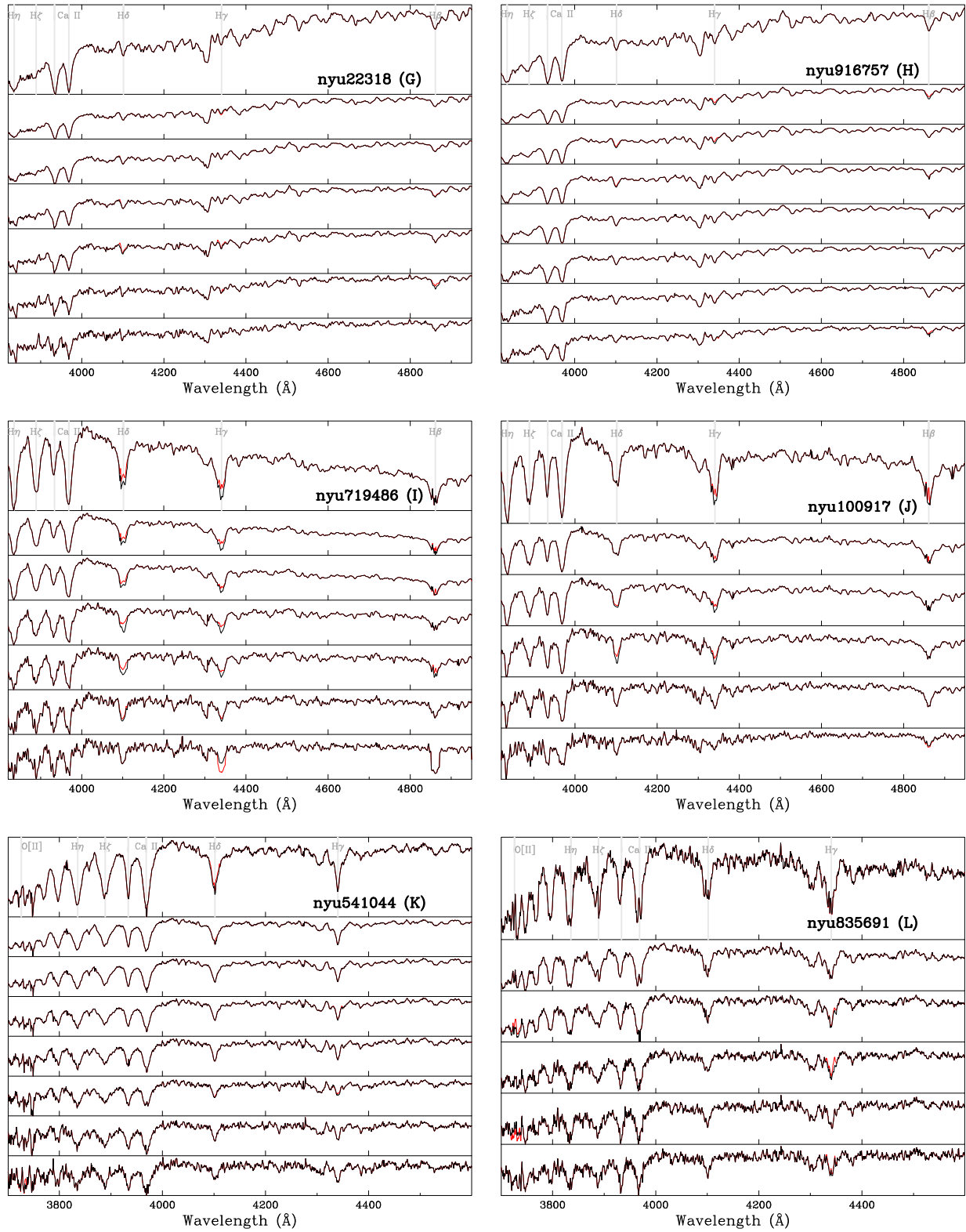
Figure C1 – *continued*

This paper has been typeset from a TEX/LATEX file prepared by the author.